AFRL-RY-WP-TR-2008-1167

BIPOLAR CASCADE EMITTERS FOR RADIO-FREQUENCY AND ELECTRO-OPTICAL APPLICATIONS

William J. Siskaninetz and Major Reginald J. Turner

Electro-Optic Components Branch
Aerospace Components and Subsystems Technology Division

MAY 2008
Final Report

Approved for public release; distribution unlimited.

See additional restrictions described on inside pages

STINFO COPY

AIR FORCE RESEARCH LABORATORY
SENSORS DIRECTORATE
WRIGHT-PATTERSON AIR FORCE BASE, OH 45433-7320
AIR FORCE MATERIEL COMMAND
UNITED STATES AIR FORCE

NOTICE AND SIGNATURE PAGE

Using Government drawings, specifications, or other data included in this document for any purpose other than Government procurement does not in any way obligate the U.S. Government. The fact that the Government formulated or supplied the drawings, specifications, or other data does not license the holder or any other person or corporation; or convey any rights or permission to manufacture, use, or sell any patented invention that may relate to them.

This report was cleared for public release by the Wright-Patterson Air Force Base (WPAFB) Public Affairs Office and is available to the general public, including foreign nationals. Copies may be obtained from the Defense Technical Information Center (DTIC) (http://www.dtic.mil).

AFRL-RY-WP-TR-2008-1167 HAS BEEN REVIEWED AND IS APPROVED FOR PUBLICATION IN ACCORDANCE WITH ASSIGNED DISTRIBUTION STATEMENT.

*//Signature//

WILLIAM J. SISKANINETZ, Project Engineer
Electro-Optic Components Branch
Aerospace Components Division   `

//Signature//

THOMAS R. NELSON, Chief
Electro-Optic Components Branch
Aerospace Components Division

//Signature//

DOUGHERTY, GEORGE, M., Major, USAF
Acting Deputy Chief, Aerospace Components Division
Sensors Directorate

This report is published in the interest of scientific and technical information exchange, and its publication does not constitute the Government's approval or disapproval of its ideas or findings.

*Disseminated copies will show "//Signature//" stamped or typed above the signature blocks.

REPORT DOCUMENTATION PAGE

Form Approved
OMB No. 0704-0188

1. REPORT DATE *(DD-MM-YY)* May 2008	2. REPORT TYPE Final	3. DATES COVERED *(From - To)* 02 January 2007 – 30 May 2008	
4. TITLE AND SUBTITLE BIPOLAR CASCADE EMITTERS FOR RADIO-FREQUENCY AND ELECTRO-OPTICAL APPLICATIONS		5a. CONTRACT NUMBER In-house	
		5b. GRANT NUMBER	
		5c. PROGRAM ELEMENT NUMBER 62204F	
6. AUTHOR(S) William J. Siskaninetz and Major Reginald J. Turner		5d. PROJECT NUMBER 2002	
		5e. TASK NUMBER IH	
		5f. WORK UNIT NUMBER 2002IH0N	
7. PERFORMING ORGANIZATION NAME(S) AND ADDRESS(ES) Electro-Optic Components Branch (AFRL/RYDP) Aerospace Components and Subsystems Technology Division Air Force Research Laboratory, Sensors Directorate Wright-Patterson Air Force Base, OH 45433-7320 Air Force Materiel Command, United States Air Force		8. PERFORMING ORGANIZATION REPORT NUMBER AFRL-RY-WP-TR-2008-1167	
9. SPONSORING/MONITORING AGENCY NAME(S) AND ADDRESS(ES) Air Force Research Laboratory Sensors Directorate Wright-Patterson Air Force Base, OH 45433-7320 Air Force Materiel Command United States Air Force		10. SPONSORING/MONITORING AGENCY ACRONYM(S) AFRL/RYDP	
		11. SPONSORING/MONITORING AGENCY REPORT NUMBER(S) AFRL-RY-WP-TR-2008-1167	

12. DISTRIBUTION/AVAILABILITY STATEMENT
Approved for public release; distribution unlimited.

13. SUPPLEMENTARY NOTES
Report contains color.

PAO Case Number: WPAFB 08-3832, 26 Jun 2008.

14. ABSTRACT

This final report details the development of two unique bipolar cascade emitter devices for radio frequency and electro-optical applications. The first device is a bipolar cascade vertical cavity surface emitting laser designed to demonstrate high slope efficiency (~1 W/A) and high-speed operation (>5 GHz). This device was developed to provide a direct-drive source for RF photonic link applications. The second device is a bipolar cascade light emitting diode designed to demonstrate a broad-area high-brightness light source for a hybrid range-intensity sensor.

15. SUBJECT TERMS
Photonic, bipolar

16. SECURITY CLASSIFICATION OF:			17. LIMITATION OF ABSTRACT: SAR	18. NUMBER OF PAGES 94	19a. NAME OF RESPONSIBLE PERSON (Monitor) William J. Siskaninetz
a. REPORT Unclassified	b. ABSTRACT Unclassified	c. THIS PAGE Unclassified			19b. TELEPHONE NUMBER *(Include Area Code)* N/A

Standard Form 298 (Rev. 8-98)
Prescribed by ANSI Std. Z39-18

i

Table of Contents

List of Figures

List of Tables

List of Abbreviations

BIPOLAR CASCADE EMITTERS

FOR RADIO-FREQUENCY

AND

ELECTRO-OPTICAL APPLICATIONS

I. Introduction

This final report details the development of two unique bipolar cascade (BC) emitter devices for radio-frequency (RF) and electro-optical (EO) applications. The first device is a bipolar cascade vertical-cavity surface-emitting laser (BC VCSEL) designed to demonstrate high slope efficiency ($\sim$1 W/A) and high-speed operation ($>$5 GHz). This device was developed to provide a direct-drive source for RF photonic link applications. The second device is a bipolar cascade light emitting diode (BC LED) designed to demonstrate a broad-area high-brightness light source for a hybrid range-intensity sensor (HRIS).

Chapter II details the development of the BC VCSEL. The design and modeling of the BC VCSEL is presented including the initial development of the broad area BC LED. Results achieved for a three-stage BC VCSEL included 7.4 GHz small-signal modulation and a slope efficiency of 0.46 W/A at an environmental temperature of -50 °C and room temperature small-signal modulation of 3.4 GHz. The detailed development for the BC VCSELs are reported in W. J. Siskaninetz's AFIT dissertation [31].

Chapter III details the development of the high-brightness BC LEDs. This research experimentally determined the maximum extent of $\sim$140 μm a TJ can be used to uniformly inject holes into a broad area device. It also detailed the design for BC resonant-cavity (RC) LED to be used as the light source for the HRIS. The detailed development for the BC LEDs are reported in R. J. Turner's AFIT dissertation [33]

II. Bipolar Cascade Vertical-Cavity Surface-Emitting Lasers for RF Photonic Link Applications

2.1   Introduction

The AFRL has been successfully designing and growing GaAs-based edge-emitting and VCSELs for Air Force applications since the mid 1990s [25] [23] [15]. The incorporation of multiple active regions into a VCSEL structure is a complicated endeavor because it significantly increases device growth times. These long growth times introduce drift considerations in the growth rates, material layer composition, and combinations of both. A migration to a VCSEL structure rather than an edge-emitting structure is required for single-spatial mode emission in a BCL incorporating more than two stages. This chapter presents details on the design and fabrication of such BC VCSELs to meet the demands of such a device to be employed as a direct-drive laser for use in an RF-Link system.

The methodology employed in the development of the BC VCSELs studied in this chapter is as follows: (1) Design a $\frac{5}{2}\lambda$ microcavity that includes a three-QW active region (AR), a tunnel junction (TJ), and an oxide aperture (OA), then fix the microcavity to develop a modular format to rapidly develop designs for simulation. (2) Model, grow, fabricate, and characterize BC LEDs to determine the best microcavity to incorporate into a BC VCSEL structure. This avoided the long growth times, as well as provided a rapid prototype to investigate. (3) Grow, fabricate, and characterize high-speed BC VCSELs. Note, semiconductor modeling is not included in the BC VCSEL characterization. AFRL and AFIT have semiconductor modeling software capable of investigating BC structures that require quantum mechanical tunneling in simple devices like BC LEDs but do not presently have the more sophisticated software for BC VCSELs.

2.2   Bipolar Cascade Vertical-Cavity Surface-Emitting Laser Cavity Design

The first step in the BC VCSEL design was to determine the cavity, resonance of a $\frac{5}{2}\lambda$ cavity placing the triple quantum well AR in a intensity resonance antinode, and the TJ and OA in a intensity resonance node. The cavity designs were created using in-house developed code. These design software routines allowed for rapid development of numer-

ous BC VCSEL structures. Placing the three functions (AR, TJ, and OA) with the required material compositions and thicknesses included into the microcavity yielded a 6950 Å thick microcavity. To rapidly model different BC microcavity designs, the microcavity was divided into modules. Since the microcavity is a $\frac{5}{2}\lambda$ cavity, nine $\frac{\lambda}{4}$ modules, with a thickness of 695 Å and two $\frac{\lambda}{8}$ modules, with a thickness of 347.5 Å were constructed. The two $\frac{\lambda}{8}$ and six of the $\frac{\lambda}{4}$ modules consisted of undoped GaAs. The three remaining $\frac{\lambda}{4}$ modules were designed to be an AR, TJ, and OA module. Figure 2.1 is a schematic illustrating the modular structure for a $\frac{5}{2}\lambda$ microcavity. The AR module consisted of a 127.5 Å thick undoped GaAs layer, three 80 Å thick $In_{0.2}Ga_{0.8}As$ QWs separated by two 100 Å thick GaAs barriers, and another 127.5 Å thick undoped GaAs layer. The TJ module consisted of a 147.5 Å thick undoped GaAs layer, the 400 Å thick GaAs TJ, and another 147.5 Å thick undoped GaAs layer. The OA module consisted of a 17.5 Å thick undoped GaAs layer, a 180 Å thick $Al_xGa_{1-x}As$ graded layer with x increasing from 0.1 to 0.9, the 300 Å thick $Al_{0.98}Ga_{0.02}As$ OA, a 180 Å thick $Al_xGa_{1-x}As$ graded layer with x decreasing from 0.9 to 0.1, and another 17.5 Å thick undoped GaAs layer.
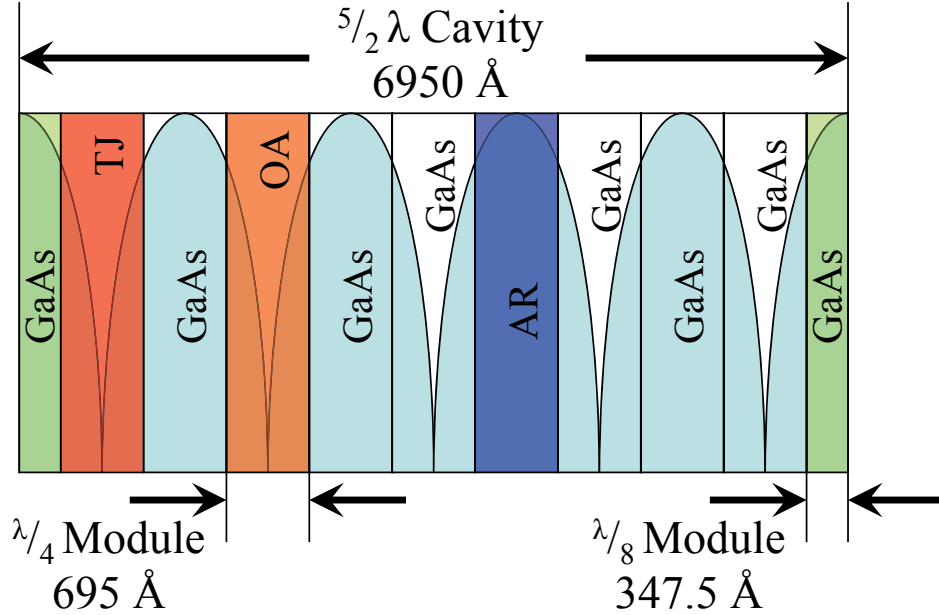
Figure 2.1: Schematic of the modular design of a $\frac{5}{2}\lambda$ microcavity. The intensity resonance profile is illustrated in light blue. There are six GaAs $\frac{\lambda}{4}$ (uncolored) and two $\frac{\lambda}{8}$ (green) modules, and one module of TJ (red), OA (orange), and AR (dark blue).

With this modular construction, the placement of each function could be quickly implemented. No changes with the GaAs and AR modules were ever required except for node and antinode (especially for the AR) placement within the microcavity. For the TJ module, care was required to ensure the hole injector, the p-doped TJ layer, was always placed nearest the AR, as well as ensuring the module was over a node. For the OA module, care was required to ensure the doping was appropriate for its placement and the module was over a node. For example, if the OA module is located between the AR and the hole-injecting TJ modules, the OA within the module must be p-doped.

Figures 2.2 a) and b) are full designs for the standard p-i-n and 1-stage BC VCSEL structures with the OA placed in the location where it can be either p-doped or undoped. All structures, p-i-n, 1-, 2-, and 3-stage, have 26.5 mirror pairs for the bottom DBR reflector and 15 mirror pairs for the top DBR reflector. The first structure, Figure 2.2 a), is a "standard" p-i-n VCSEL with the active region and undoped OA in the same location of the field intensity profile as the BC VCSELs. Figure 2.2 b) is a 1-stage BC VCSEL with both of the DBR mirror stacks Si-doped. The tunnel junction is in the node nearest the top DBR to act as the hole injector for this structure and the OA is in the next adjacent node. The 2- and 3-stage designs are identical to the 1-stage design except the microcavity is repeated two and three times, respectively. The blue traces are the layer index profiles; the red traces are the field intensities; and the black traces are normalized power densities. The power density is developed throughout the entire device by considering absorbed and "generated" top and bottom emitted powers, and integrating them with the field - index product over all of the layers. The "normalized" power density traces have been scaled to fit on the intensity axis. The "zero" axis is set to be two on the intensity axis for ease in viewing. This power density calculation provides valuable insight into the number of QWs that can be used within a resonance antinode.

Figure 2.3 shows zoomed-in views of the microcavity design for a) a p-i-n VCSEL, b) a 1-stage BC VCSEL, c) a 2-stage BC VCSEL, and d) a 3-stage BC VCSEL. Using a three-quantum well active region centered in a field intensity antinode results in less than a 10% decrease in power of the outer QWs compared to the middle QW. These designs show

4
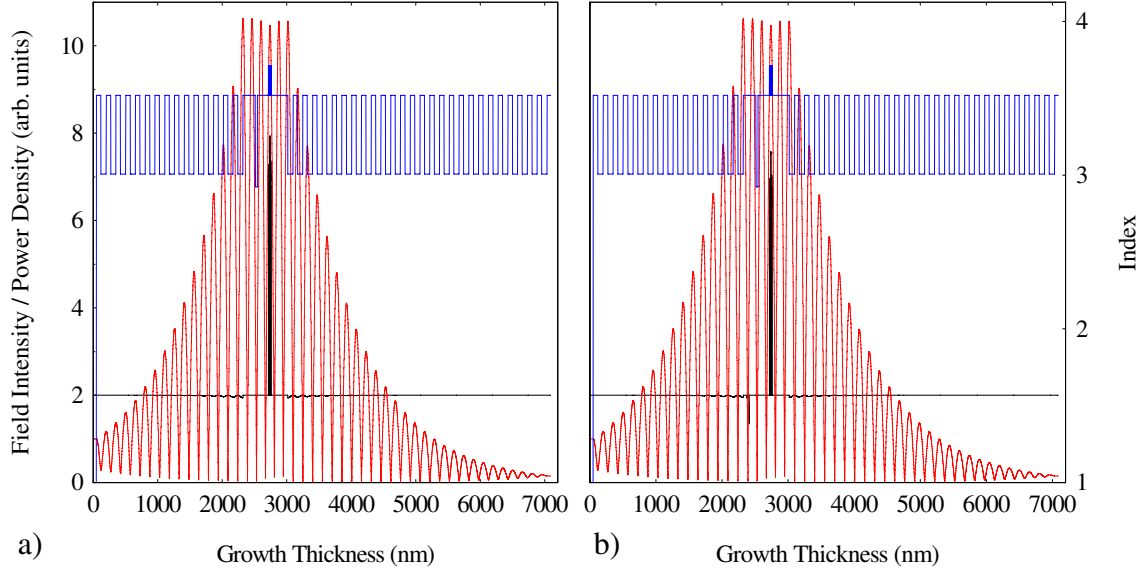
Figure 2.2: Standard and BC VCSEL designs a) is the standard *p-i-n* VCSEL and b) is the 1-stage BC VCSEL. The blue traces are the layer index profiles; the red traces are the electric field intensities; and the black traces are power densities.

an interesting improvement opportunity to reduce device losses. The p-doped tunnel junction layer shows a large loss in the power density. Shifting the TJ slightly to the left so the higher loss p-doped TJ layer is closer to the cavity node will reduce scattering losses. While it would be expected the n-doped TJ layer would exhibit increased scattering losses, these losses will be significantly less because the p-doped TJ layer has nearly an order of magnitude higher doping than the n-doped TJ layer. Also, per decade of doping, the p-doping losses are much larger than n-type losses. Combined with the higher doping concentration, a compounded loss effect that can really negatively impact device performance is achieved.

2.3 *Bipolar Cascade Light Emitting Diode Modeling*

With the definition of the BC VCSEL microcavity complete, the modeling of BC LEDs was initiated. Investigating BC LEDs instead of BC VCSELs initially provided a first step that disentangled the physics of the microcavity in BC VCSELs from the additional complications that result from laser operation in a similar BC VCSEL structure. Semiconductor and optoelectronic modeling was accomplished with APSYS software from
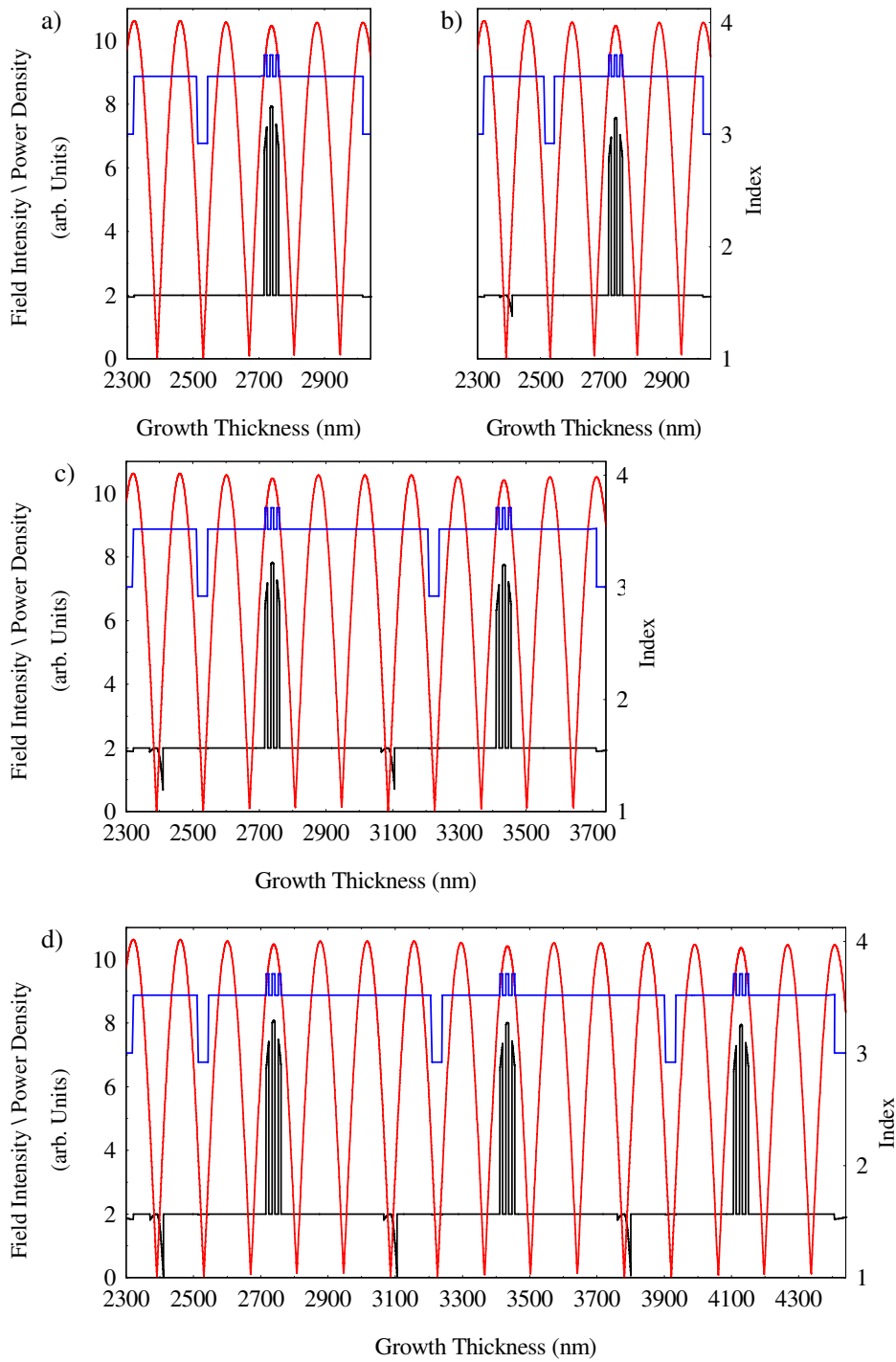
Figure 2.3: Standard and BC VCSEL microcavity designs a) is the standard *p-i-n* VC-SEL, b) the 1-stage BC VCSEL, c) the 2-stage BC VCSEL, and d) the 3-stage BC VCSEL. The blue traces are the layer index profiles, the red traces are the electric field intensities, and the black traces are a power density plot.

Crosslight and included, at a minimum, band structure, VI, and LI simulations for LED structures. This software allowed for the investigation of LED structures with applied bias and injected current. Unbiased and biased band diagrams were developed for the *p-i-n* LED, and 1-, 2-, and 3-stage BC LEDs with undoped, n-type, and p-type OAs. VI and LI characteristics were also modeled and will be discussed in Section 2.4.3.

Figure 2.4 is the band diagram for the *p-i-n* LED with an n-doped OA. Figures 2.5, 2.6, and 2.7 are band diagrams comparing 1-stage , 2-stage, and 3-stage BC LEDs, respectively, with a) undoped, b) n-doped, and c) p-doped OAs. For the p-doped designs the order of the microcavity was changed so the hole injector was always on the valence band side of the QWs. For all these designs, the first 0.5 μm is the n-doped GaAs substrate. For the BC LEDs, the microcavity is sandwiched between 0.2 μm thick layers of n-doped GaAs, and for the *p-i-n* LED, the microcavity is sandwiched between a 0.2 μm thick n-doped GaAs layer next to the GaAs substrate and a 0.2 μm thick p-doped GaAs layer on top.

By n-doping the OA, several benefits were immediately identified: (1) n-doping the OA dramatically reduced the required potential to flatten the bands. For a 1-stage device, the reduction was greater than 0.75 V. (2) The electron barrier in the conduction band was eliminated, thereby allowing more electrons to fill the quantum wells. (3) A hole barrier in the valence band was created, allowing greater hole accumulation around the QW region. This effect has not been discussed in the literature until this research reported it [27].

The improvements that are readily apparent by using a p-doped OA were (1) the increased region for hole accumulation in the valence band and (2) an electron barrier in the conduction band. Since electron mobility is significantly greater than hole mobility, the slight increase in the conduction band slope is greatly offset by the capability to accumulate a significantly greater number of holes in the valence band.

These diagrams provide tremendous evidence for p-doped OAs to significantly improved BC emitter performance. Comparing the band diagrams of an n-doped OA structure to a p-doped OA structure at 0 V and at a bias of 3 V yields several conclusions: (1) At 3 V, the p-doped OA has a 0.75 eV electron barrier in the conduction band, whereas in the

n-doped OA, there is nothing to restrict electrons not captured by the QWs from continuing on and dropping down into the next stage. This is detrimental to the initial stage because, as those electrons travel to the next stage, they are restricting hole generation because fewer valence band electrons in the first stage are able to tunnel into the conduction band of the subsequent stage. (2) At the 50 mA bias, the p-doped OA tunneling region is $\sim$0.5 eV and the n-doped OA tunneling region is $\sim$0.1 eV. This higher region increases the number of states to which valence band electrons can tunnel and become conduction band electrons for subsequent stages.

2.4 *Bipolar Cascade Light Emitting Diodes*

2.4.1 Introduction.   Single-cavity BC VCSELs and LEDs have shown great promise for increasing device slope efficiency and differential quantum efficiency by epitaxially connecting in series ARs with reverse-biased TJs [9, 12]. As with conventional *p-i-n* junction VCSELs, a common design feature of the BC variety is an OA that serves to funnel the injected current toward the center of the active region for better fundamental optical mode and gain overlap. While the AR and the TJ have been studied extensively and optimized to improve device performance, the only considerations typically mentioned in the literature for the OA are optimum placement at nodes of the cavity resonance, material grading, tapering, and layer thickness. However, doping of the OA within the microcavity has not been discussed to the best of the author's knowledge. This section discusses how doping the OAs placed inside the microcavity of single- or multiple-stage BC LEDs significantly improves overall device performance by reducing the operating voltage, increasing the light power, and reducing junction heating.

OA layers are routinely doped when they are located within a DBR stack in *p-i-n* junction VCSEL and 1-stage BC VCSEL structures [2, 35]. Generally, in single-cavity multiple-AR BC structures, undoped OAs are located within the mostly undoped (except for the degenerately doped tunnel junction layers) microcavity. The OA layers within the microcavity have been shown to reduce bistability effects due to current spreading between successive active regions [13]. Doping the microcavity OAs generally increases losses due

8
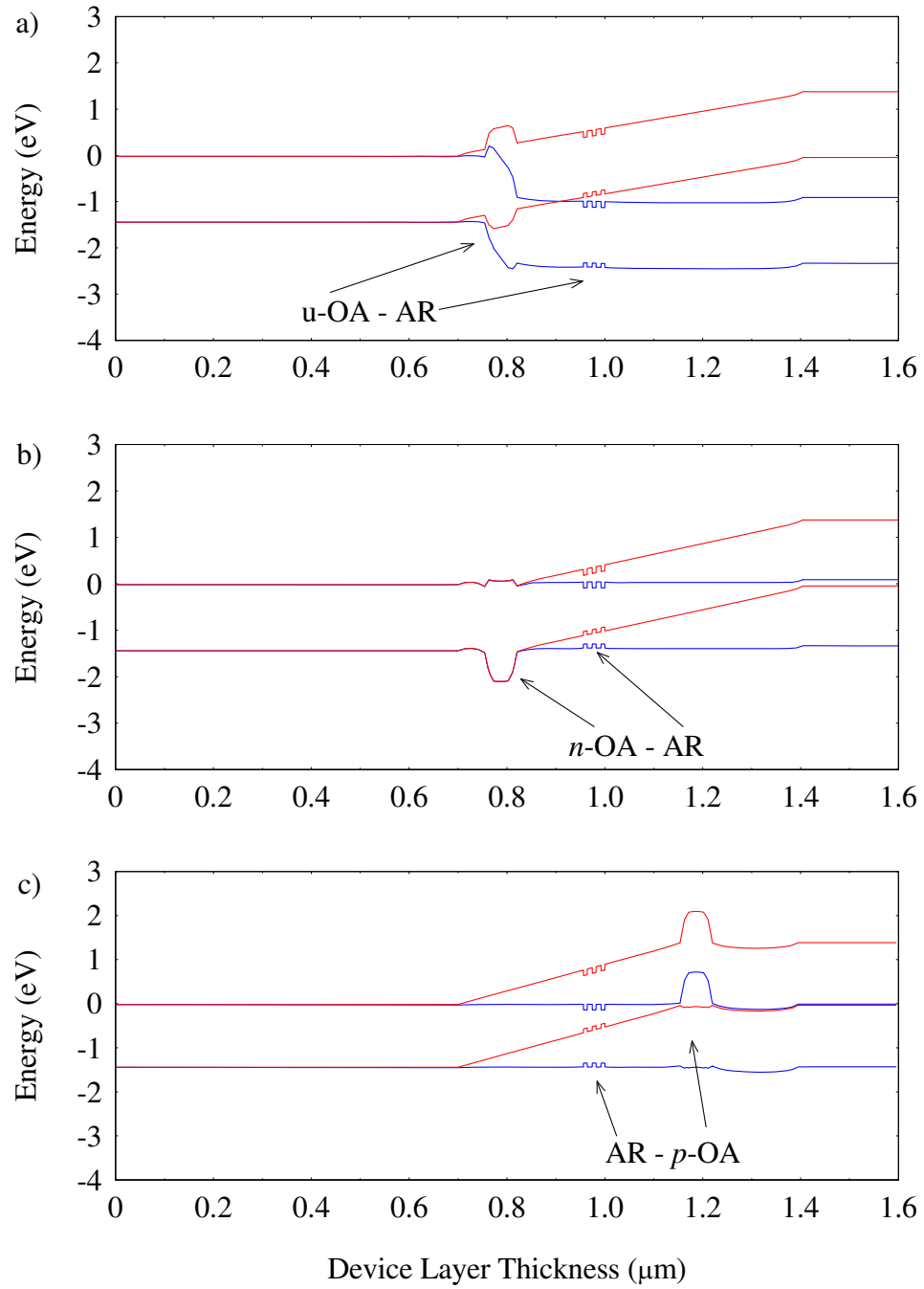
Figure 2.4: Energy band diagrams comparing *p-i-n* LEDs with undoped, n-doped and p-doped OAs. The red energy bands are at 0 V and the blue energy bands are at an injection current of 50 mA.
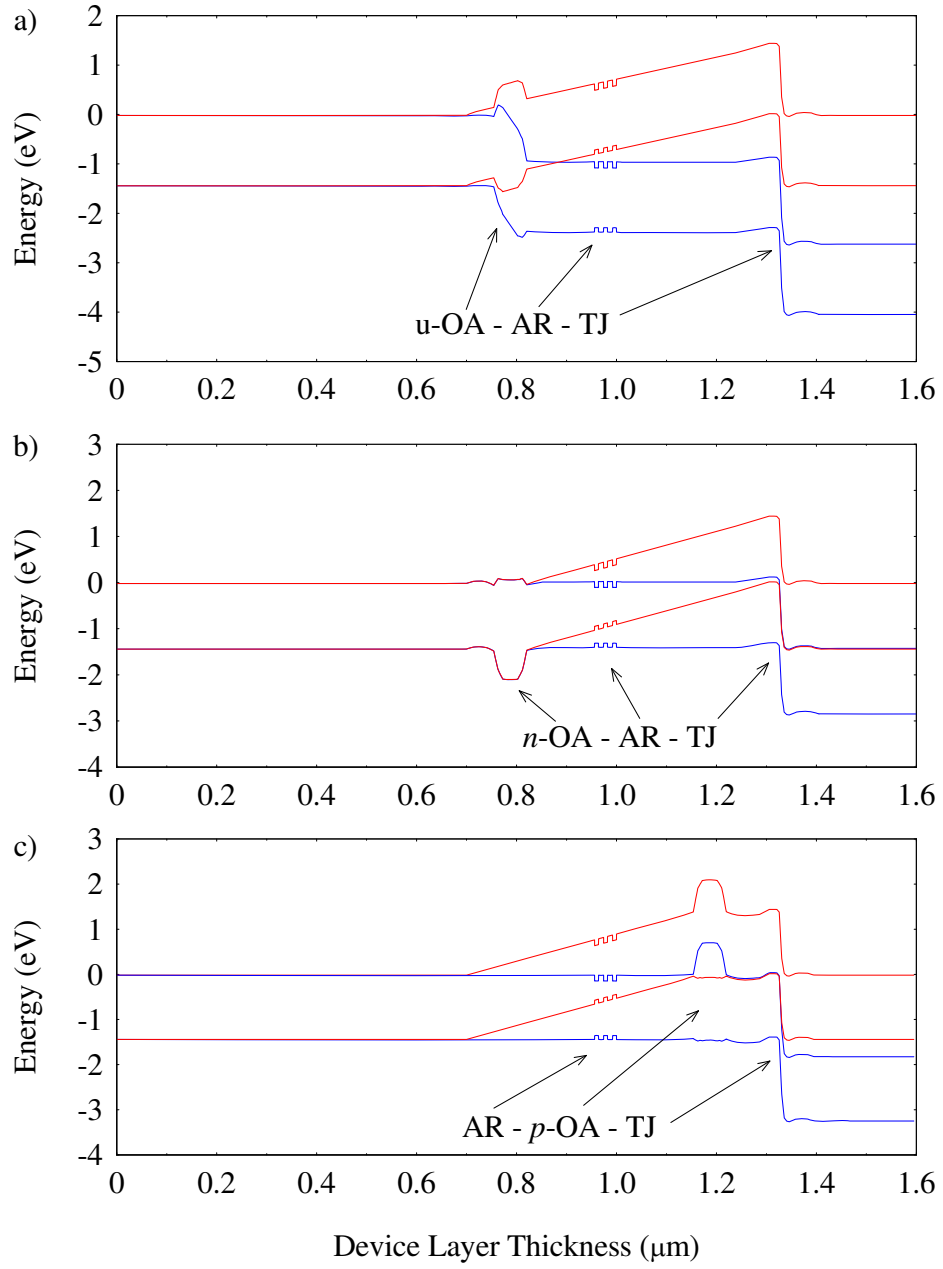
Figure 2.5:   Energy band diagrams comparing 1-stage BC LEDs with undoped, n-doped and p-doped OAs. The red energy bands are at 0 V and the blue energy bands are forward biased at an injection current of 50 mA.
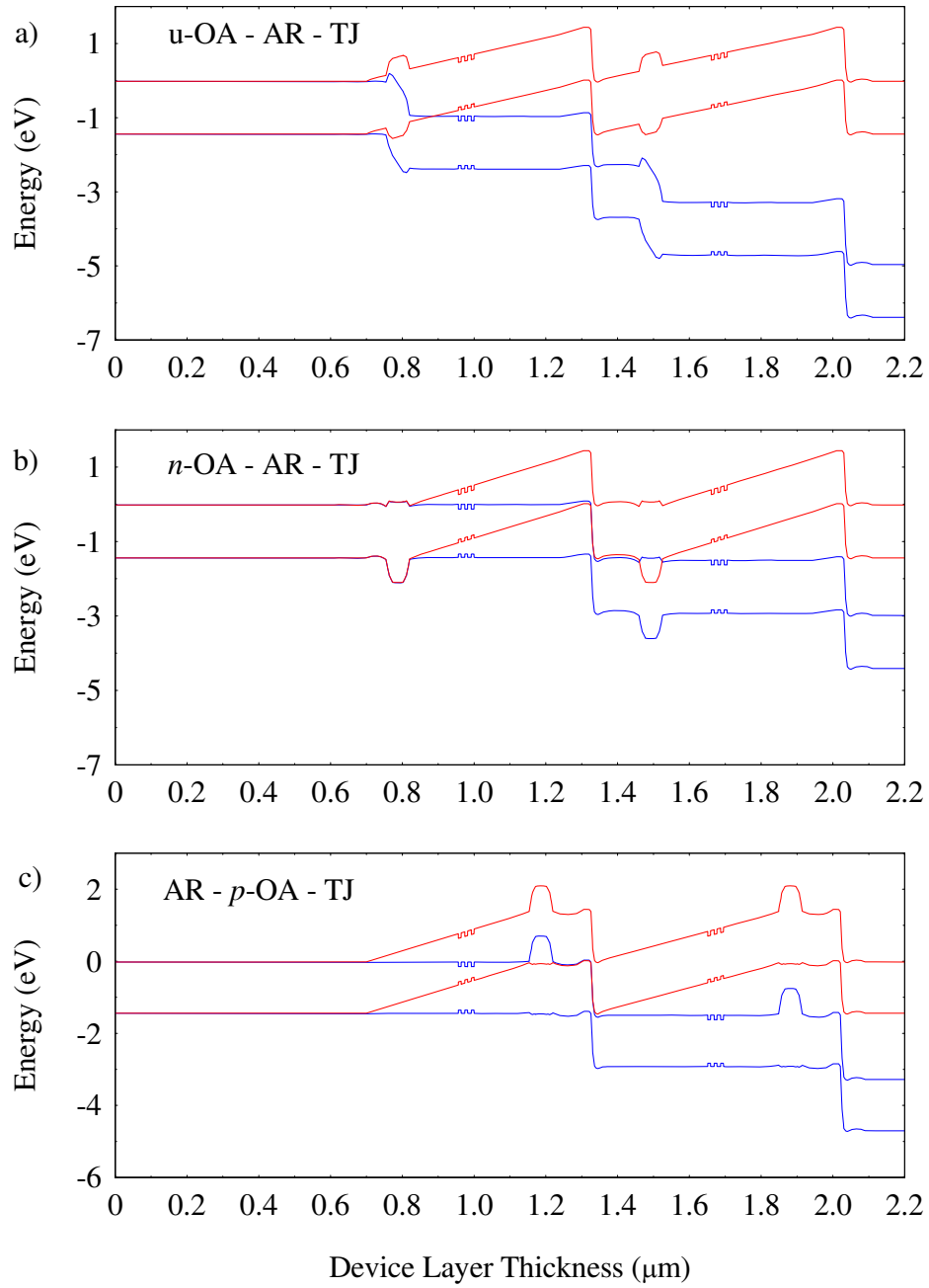
Figure 2.6: Energy band diagrams comparing 2-stage BC LEDs with undoped, n-doped and p-doped OAs. The red energy bands are at 0 V and the blue energy bands are forward biased at an injection current of 50 mA except for the 2-stage p-doped OA BC LED which is at 48 mA. This is due to computational instabilities and software version incompatibilities that did not allow the APSYS software to completely model the 2-stage BC LED across the full 50 mA current range.
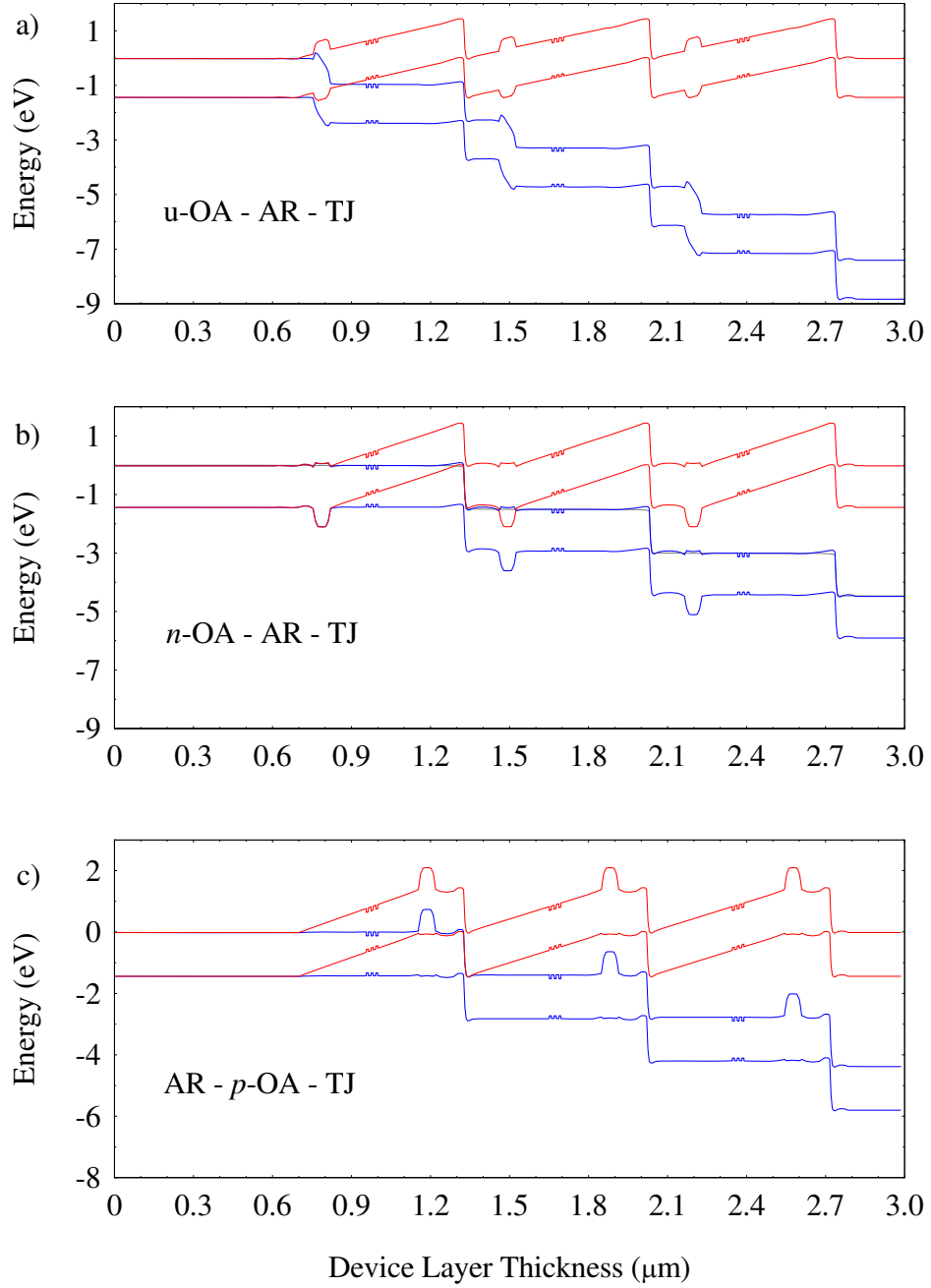
Figure 2.7:   Energy band diagrams comparing 3-stage BC LEDs with undoped, n-doped and p-doped OAs. The red energy bands are at 0 V and the blue energy bands are forward biased at an injection current of 50 mA except for the 3-stage p-doped OA BC LED which at a low voltage bias of 4.3 V, which corresponds to less than 1 mA. This low bias is due to computational instabilities and software version incompatibilities that did not allow the APSYS software to completely model the 3-stage BC LED across the full 50 mA current range.

to scattering and free-carrier absorption. However, with proper insertion in the cavity in a resonance node, much of the loss can be avoided. These losses will be shown to be much less than the gains achieved by doping the OAs.

This investigation focuses on the OA layers and the evolution of the experiment designed around a systematic series of BC LED structures, similar to that shown in the lower panel of Figure 2.8. This structure allows the physics of the microcavity in BC devices to be disentangled from the additional complications that result from laser operation in a similar BC VCSEL structure [**?**].
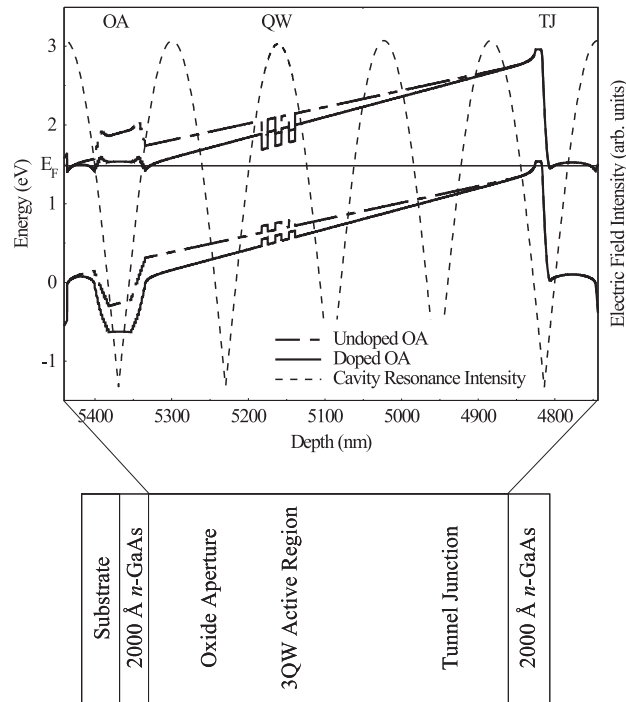
Figure 2.8: Calculated electric-field intensity (dashed lines) and real-space energy band diagrams of a single-stage BC VCSEL with undoped (semi-dashed lines) and doped ($N_d = 2 \times 10^{18}$ cm^{-3}) OAs (solid lines) in and around the microcavity active region (the top and bottom DBRs are not shown). Also shown is a schematic diagram of a single-stage BC LED device with the BC VCSEL microcavity [27].

2.4.2 Bipolar Cascade Light Emitting Diode Growth & Fabrication. To investigate the electrical, optical, and electroluminescent (EL) properties of the microcavities, BC LEDs were grown by moleculear beam epitaxy (MBE) in a Varian Gen II system on n-type (100) GaAs substrates consisting of a microcavity designed to be in a $\frac{5}{2}\lambda$ thick *p-i-n* VC-

SEL or a BC VCSEL structure with 1-, 2-, or 3-stages. Initially, seven LED (*p-i-n* and BC) structures were grown to quickly evaluate the affects of doping the OA, as well as to determine if thicker TJ layers would be beneficial to BC LED performance. The microcavity is stacked between 2000 Å thick GaAs cladding layers. The *p-i-n* LEDs top cladding layer is C-doped at 4×10^{18} cm^{-3} and the bottom cladding is Si-doped at 4×10^{18} cm^{-3}. The BC LED's cladding layers are both Si-doped at 4×10^{18} cm^{-3}. A 1-stage undoped/*n*-doped BC LED device is shown schematically at the bottom of Figure 2.8. Each $\frac{5}{2}\lambda$ thick stage consists of a graded OA located in the first node (left to right in Figure 2.8), a triple QW active region located in the third antinode, and a tunnel junction located in the fifth node of the cavity resonance. Placing the OAs and tunnel junctions in the nodes minimizes losses and placing the QW in the antinode maximizes the gain achieved from the cavity. The graded OAs consist of a 180 Å thick Al$_x$Ga$_{1-x}$As layer with x increasing from 0.1 to 0.9, a 300 Å thick Al$_{0.98}$Ga$_{0.02}$As OA (undoped for the *p-i-n*, 1- and 2-stage BC LEDs and *n*-doped at 2×10^{18} cm^{-3} for the 3-stage BC LED), and a 180 Å thick Al$_x$Ga$_{1-x}$As layer with x decreasing from 0.9 to 0.1. The AR has three 80 Å thick In$_{0.20}$Ga$_{0.80}$As QWs separated by 100 Å thick GaAs barriers. The GaAs TJ consisted of a p^{++} layer C-doped at 5×10^{19} cm^{-3} and an n^{++} layer Si δ-doped with an effective doping level of $\sim 2 \times 10^{19}$ cm^{-3}. The TJ layers were either 100 Å or 200 Å thick to investigate the minimum layer thickness required for optimal device performance. Additional TJ growth details appear elsewhere [25].

The next series of crystal growth consisted of five samples grown consecutively to fill in the comparison matrix between undoped and *n*-doped OA BC LEDs. The five samples all had 200 Å thick TJ layers because, as seen in Section 2.4.3, the BC LEDs with 200 Å thick TJ layers significantly outperformed the BC LEDs with 100 Å thick TJ layers with respect to light output. The final series of crystal growth consisted of the *p*-doped OA BC LEDs. Table 2.1 encapsulates the LEDs developed for this study, detailing the time line of sample growth, if the devices were modeled or grown, what the OA doping level was, and the TJ layer thickness. The last two structures in Table 2.1 were modeled for completeness but never grown because *p-i-n* structures were not necessary because any information obtained would not influence the BC structures.

Although the MBE is constantly being recalibrated to ensure ternary compositions and growth rates are well defined, due to the system complexity changes in the MBE system make it very difficult to keep the uncertainty of the InGaAs composition and growth rate to a minimum. The ternary growth is always "best effort" because for a research effort like this device research would rapidly become cost prohibitive. This makes defining a QW to emit at 980 nm to be an uncertain process. This will be seen in the electroluminescence characterization illustrated in this chapter.

Table 2.1: Modeling and Growth details for *p-i-n* and BC LED structures. The lines separate the growth runs. The first seven samples were grown consecutively, the next four samples were grown at a later date consecutively, and the last three samples were grown consecutively.

Structure	Modeled	Grown	OA Doping Concentration	TJ Layer Thickness
	Y/N	Y/N	$(10^{18}$ cm$^{-3})$	(Å)
p-i-n n-doped OA	Y	Y	2	No TJ
1-Stage n-doped OA	N	Y	2	100
1-Stage n-doped OA	Y	Y	2	200
2-Stage n-doped OA	N	Y	2	100
2-Stage n-doped OA	Y	Y	2	200
3-Stage Undoped OA	N	Y	Undoped	100
3-Stage Undoped OA	Y	Y	Undoped	200
3-Stage n-doped OA	Y	Y	2	200
4-Stage n-doped OA	N	Y	2	200
1-Stage Undoped OA	Y	Y	Undoped	200
2-Stage Undoped OA	Y	Y	Undoped	200
1-Stage p-doped OA	Y	Y	2	200
2-Stage p-doped OA	Y	Y	2	200
3-Stage p-doped OA	Y	Y	2	200
p-i-n Undoped OA	Y	N	Undoped	No TJ
p-i-n p-doped OA	Y	N	2	No TJ

The samples were processed into LEDs with square mesas and 5 μm-wide square annulus top metal contacts 5 μm inside the perimeter of the mesa. The top and bottom (backside metal) ohmic contacts consist of a Ni:Ge:Au:Ni:Au metal layer profile that was annealed in forming gas (95% Ar - 5% H$_2$) at 410 °C for 15 seconds. Each device was dry etched using a BCl$_3$-Cl$_2$ recipe through the active region to form isolation mesas. The OA

layers were never oxidized because these are BC LEDs and the investigation was to study the effects of doping the AlGaAs OA layer and not the oxidized material.

2.4.3   Bipolar Cascade Light Emitting Diode Characterization.   LED characterization consisted of VI, LI, EL, and intensity characterization. Room temperature VI and LI characterization was performed using a Cascade Microtech probe station, an HP 4145A semiconductor parameter analyzer (SPA), and a 1 cm diameter Si *p-i-n* photodetector positioned above the needle probe to maximize light collection across the entire current range. Since the photodetector was above the probe, the collected light values are maximized relative values not absolute values. The EL characterization used the SPA as the constant current source operating at 50 mA; the output light was coupled into a silica multimode fiber (core diameter of 63 μm) aligned to maximize the collected light and measured using an HP 70951B optical spectrum analyzer. Again, the power values are maximized relative values and not absolute values. The intensity characterization used the SPA as the constant current source operating at 50 mA; the LEDs were imaged using a Spiricon 980M near-infrared camera and image capture software. The camera was operated with linear gain and not auto-gain compensation, allowing all images to be compared directly.

Initial characterization, shown in Figure 2.9, indicated significant improvement in both voltage and light performance with n-doped OAs. The 1- and 2-stage devices scaled at nearly 1.5 V. This is slightly higher than a typical 980 nm InGaAs QW LED which has an average operating voltage of 1.2 V. The increase can be attributed to the TJ and OA. However, the 3-stage undoped device scaled at $\sim$2.7 V, caused almost entirely by the undoped OA creating a conduction band electron barrier discussed in Section 2.3. It is also clearly evident that the n-doped OA has a significant effect on the device performance in both the operating voltage, as well as the light output characteristics.

The Figures 2.10, 2.11, and 2.12 present the VI, LI and EL characterization. In all of these figures, the first panel details undoped OAs, the second panel details n-doped OAs, and the third panel details p-doped OAs. The lines are Crosslight APSYS simulation results and the data points (open circles and upsidedown triangles) are measured device

16
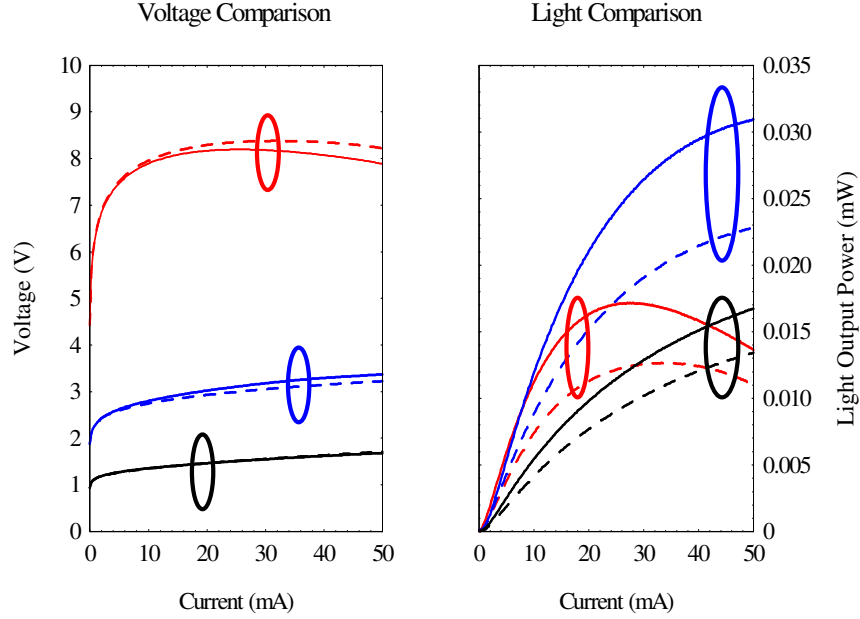
Figure 2.9: Comparison to determine the optimum tunnel junction layer thickness. The black traces are 1-stage BC LEDs; the blue traces are 2-stage BC LEDs; and the red traces are 3-stage BC LEDs. The solid-line traces are devices with 200 Å TJs and the dashed line traces are devices with 100 Å thick TJs. Voltage comparison is inconclusive; however, the light output power comparison clearly indicates the 200 Å thick layer thickness is far superior.

results. The color scheme is the same for all panels, the 1-stage devices are black, the 2-stage devices are blue, the 3-stage devices are red, the 4-stage device is green, and the *p-i-n* device is dashed black with the upsidedown triangles.

Figure 2.10 summarizes the voltage characterization, as well as simulation results for all but one of the structures. The samples all scale in voltage with increased number of stages, as expected, and all agree with simulations. The undoped OA structures deviate the most from simulations. This is believed to be due to more excessive heating in these structures that is not adequately modeled. Significant reductions in operating voltages are clearly observed for the doped-OA devices, compared to the undoped-OA devices. Nearly uniform voltage steps going from one to three BC stages are observed. This indicates that the one to three combinations of OA and TJ are the dominant series resistances, as is expected for good devices. The doped-OA devices demonstrate nearly a 50% reduction
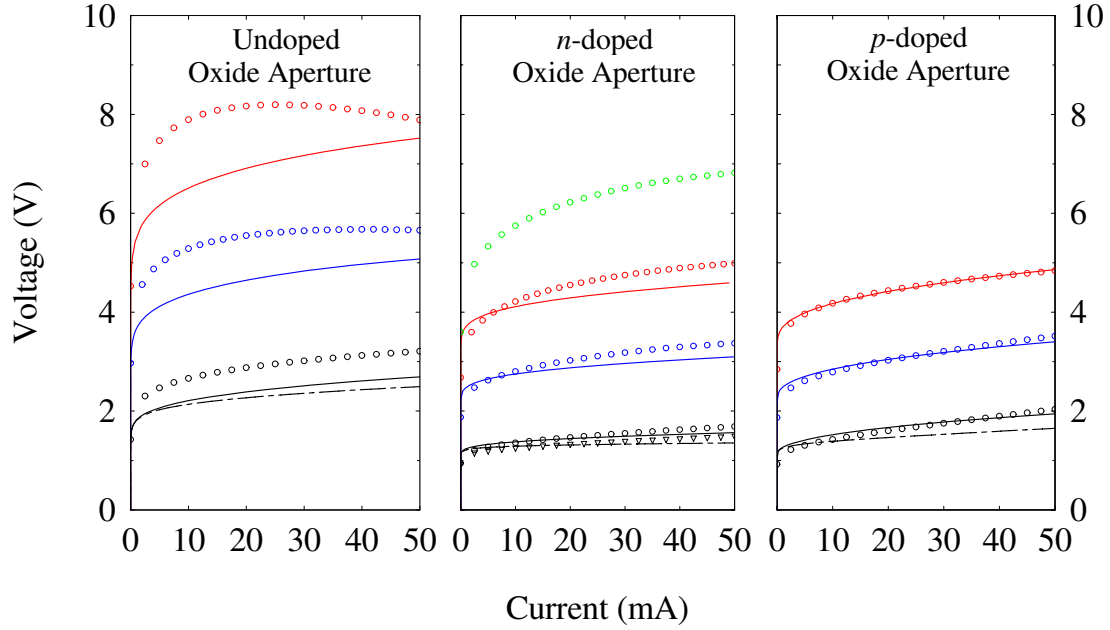
Figure 2.10: Voltage comparisons of standard and BC LEDs. The solid lines are simulation results and the points are measured device results. The color scheme is the same for all panels, the 1-stage devices are black, the 2-stage devices are blue, the 3-stage devices are red, the 4-stage device is green, and the *p-i-n* device simulation result is a dashed black line and the measured results are upsidedown triangles. The doped and undoped aperture structures all scale with the number of active regions.

in operating voltage when compared to the undoped-OA devices with the same number of stages, and is further corroborated by the simulations. The scaling between successive stages is very uniform, with about 1.5 V per stage for the doped graded OA structures and about 2.7 V per stage for the undoped-OA structures. Significantly, the 3-stage doped OA LEDs have lower operating voltages than the 2-stage undoped OA LED.

Figure 2.11 summarizes the light characterization and indicates the dramatic improvement in output light intensity that is achieved by cascading active regions as well as the improvement by doping the OAs. The undoped OA structures generate much less light as well as show thermal roll off occurring at much lower injection currents. This is evident for all numbers of device stages. The undoped and *n*-doped OA devices catastrophically failed (by blowing off the metal contacts) more readily, forcing the testing to stop at 50 mA. However, the *p*-doped devices were significantly more robust and were only limited by the SPA used to test the devices. The 2- and 3-stage devices with *n*-doped OAs have

a nearly a 160% and 200%, respectively, improvement in light power at 30 mA over the undoped OA devices.
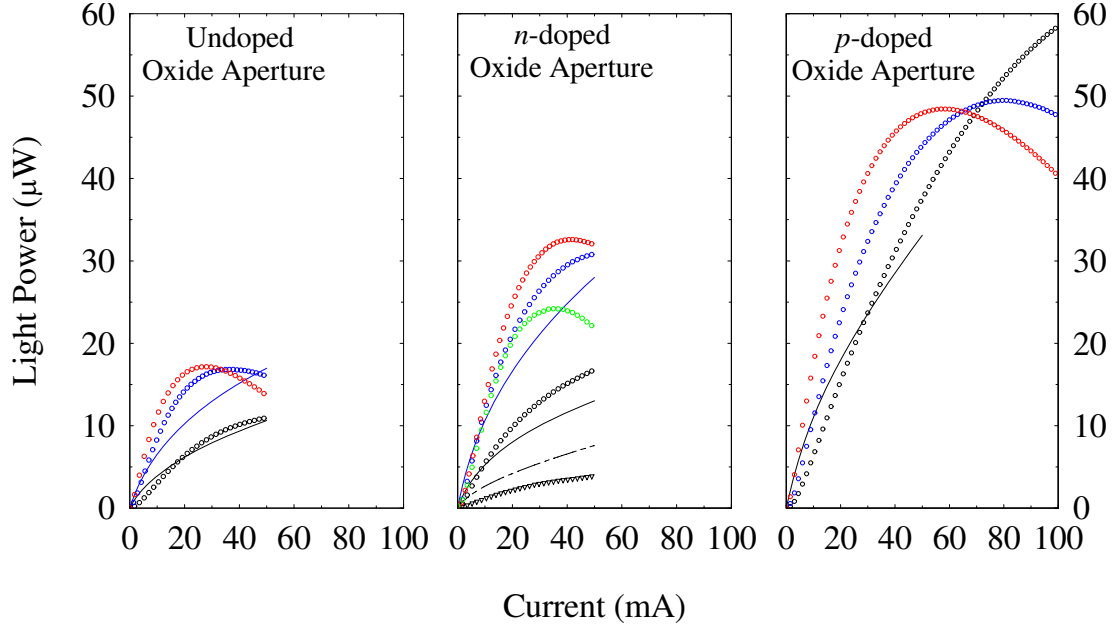
Figure 2.11:   Light output comparisons of standard and BC LEDs. The solid lines are simulation results (which were scaled appropriately) and the points are measured device results. The color scheme is the same for all panels, the 1-stage devices are black, the 2-stage devices are blue, the 3-stage devices are red, the 4-stage device is green, and the *p-i-n* device is black but with upsidedown triangles and a long dashed line. Nearly all the doped OA BC LED devices outperform the undoped OA devices.

Saturation effects are also evident in the devices due to junction heating. The LI curves of the undoped OA devices roll over at smaller current densities due to increased junction heating as a result of the larger electron injection barrier. It is also evident that there is a limit to the number of stages that can be implemented to improve the light output due to junction heating. The output power and overall power conversion efficiency of the 4-stage *n*-doped BC LED both decreased as compared to the 3-stage *n*-doped device. Table 2.2 indicates the current where the thermal saturation effects occurs for each device.

The APSYS software simulated results do not appear to predict the thermal saturation effects or light output scaling for multi-stage BC LEDs as well as it does the electrical properties for multi-stage BC LEDs. This may result from the difficulty in computationally

accounting for the increased number of electrons and holes available for optical recombination due to the barriers formed by the doped OAs.

The question arises as to why the 2- and 3-stage p-doped devices do not perform as well as the 1-stage device. Returning to the band diagrams in Figures 2.5-2.7 will provide some insight. For the 1-stage device, the number of conduction band electrons near the QWs is very large and are effectively blocked from traversing the entire length of the device by the OA. Also, the band of tunneling states is large ($\sim$0.75 eV) for valance band electrons to tunnel into the conduction band, generating holes for optical recombination, in the QWs. For multiple-stage devices, the subsequent injection of conduction band electrons is limited by the rate of optical recombination creating valence band electrons, as well as the rate valence band electrons can tunnel into the next stage. The TJs in the stages nearest the substrate exhibit relatively small bands of tunneling states ($<$0.1 eV) with the topmost TJ exhibiting the largest band of tunneling states ($\sim$0.5 eV and $\sim$0.4 eV for the 2- and 3-stage devices, respectively). Presuming the BC LED modeling is correct, it is not clearly understood why only one of the TJs band overlap increases with increased bias and not all of the TJs equally. Further investigation of this may be able to provide significant improvements in p-doped OA BC emitters. One possible avenue of investigation is to include a barrier (either a doped GaAs region or another OA) opposite the QW from the OA.

Figure 2.12 summarizes the EL for the *p-i-n* LED and the 1-, 2-, and 3-stage devices. The undoped OA samples exhibit significantly lower QW luminescence and have pronounced red shifts in the GaAs emissions as compared to the doped OA samples. These differences are attributed to greater device heating in the undoped OA samples. These shifts are tabulated in detail in Table 2.2. The GaAs peak wavelengths indicate larger red shifts per stage for the undoped OA structures ($\sim$13.5 nm) as compared to the doped OA structures ($\sim$7-9 nm). It can be argued that the EL peak will scale linearly with the number of cascaded stages for both doped and undoped OA structures. If the EL peak for the 3-stage doped structure did not suffer from heating effects, the peak would most likely scale such that the emission peak would be linear with EL peaks of the 1- and 2-stage undoped structures. Due to growth uncertainties of the InGaAs QWs the peaks may or may not follow

Table 2.2: Current at thermal rollover, EL peak wavelengths, and EL area analysis at 50 mA for doped and undoped 50 μm $\times$ 50 μm square OA devices at room temperature.

Structure	LI Peak Current (mA)	GaAs Peak (nm)	QW Peak (nm)	EL Area (arb. units)
1-Stage Undoped OA	~50	874.1	995.4	238
2-Stage Undoped OA	35.6	880.2	992.7	490
3-Stage Undoped OA	26.3	887.6	989.4	534
p-i-n *n*-doped OA	>50	872.0	974.7	78
1-Stage *n*-doped OA	≫50	872.0	972.7	360
2-Stage *n*-doped OA	>50	874.7	976.0	755
3-Stage *n*-doped OA	39.4	878.7	987.3	888
4-Stage *n*-doped OA	34.5	884.7	995.3	707
1-Stage *p*-doped OA	≫100	872.3	968.4	615
2-Stage *p*-doped OA	78.6	877.6	969.8	877
3-Stage *p*-doped OA	57.4	881.6	985.0	1150

the GaAs peaks as well. This is observed in the 3-stage undoped-OA BC LED where one can observe that the InGaAs QW peak has a shorter wavelength as compared to the 1- and 2-stage undoped OA BC LEDs. The best explanation for this is that the 1- and 2-stage undoped OA BC LED material was grown several weeks after the 3-stage undoped OA BC LED and the growth environment has changed enough to add this uncertainty.

Another interesting observation from Figure 2.12 is the appearance that more light is emitted by the n-doped OA BC LEDs than by the p-doped OA BC LEDs, in contrast to the LI results in Figure 2.11. While spectrally this is true at the design wavelength of ~980 nm, the detector used for collecting the light in Figure 2.11 collects the entire waveband of emitted light. Therefore, the total integrated output must be considered for the LI. The final column in Table 2.2 quantifies the area of each EL measurement and corroborates the LI data in Figure 2.11 very well. Then, why does the p-doped OA BC LED have a smaller and flatter peak at the design wavelength? One explanation is that the p-doped OA barrier allows for a larger number of electrons and holes to accumulate in the conduction and valence bands, respectively, thus allowing an increased bulk GaAs optical recombination. There is evidence of this in Figure 2.12; the GaAs peak for all three p-doped OA BC LED samples are appreciably larger than the two other types of BC LEDs. Another explanation
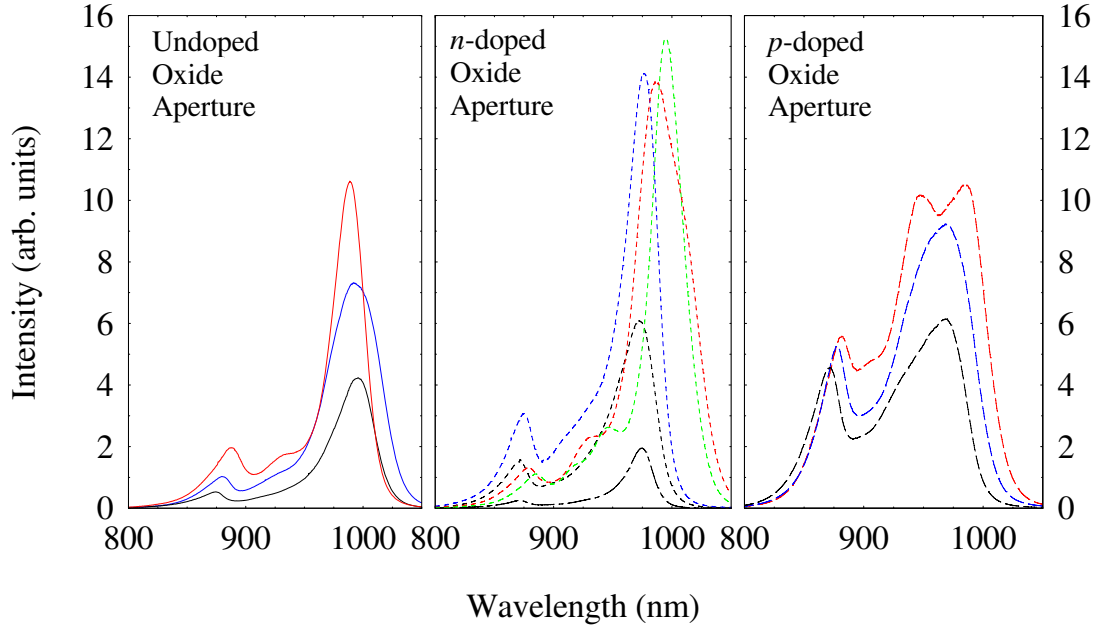
Figure 2.12: Measured EL comparisons of standard and BC LEDs at a current of 25 mA. The color scheme is the same for all panels, the 1-stage devices are black, the 2-stage devices are blue, the 3-stage devices are red, the 4-stage device is green, and the *p-i-n* device is black with a long dashed line. The doped OA BC LED devices all have stronger QW emission and do not exhibit as significant of a red shift due to device heating as the undoped OA devices.

is the p-doped OA BC LEDs were grown several months after the undoped and n-doped OA BC LEDs and environmental changes in the MBE may have affected the QWs. The broad and, in the case of the 3-stage sample, double peak of the InGaAs signature in the p-doped BC LED relative to the other BC LED InGaAs peaks in Figure 2.12 gives evidence of material growth issues.

Figure 2.13 shows the improvements in luminescence uniformity between a *p-i-n* LED and a single-stage BC LED with n-doped OAs at an operating current of 50 mA under identical image capture conditions. With the standard *p-i-n* junction LED, it is evident that the luminescence is limited to the region around the top metal contact, whereas the single-stage BC LED luminescence profile is significantly more uniform. The improvement is due to uniform spreading of the higher mobility electrons across the whole LED mesa in
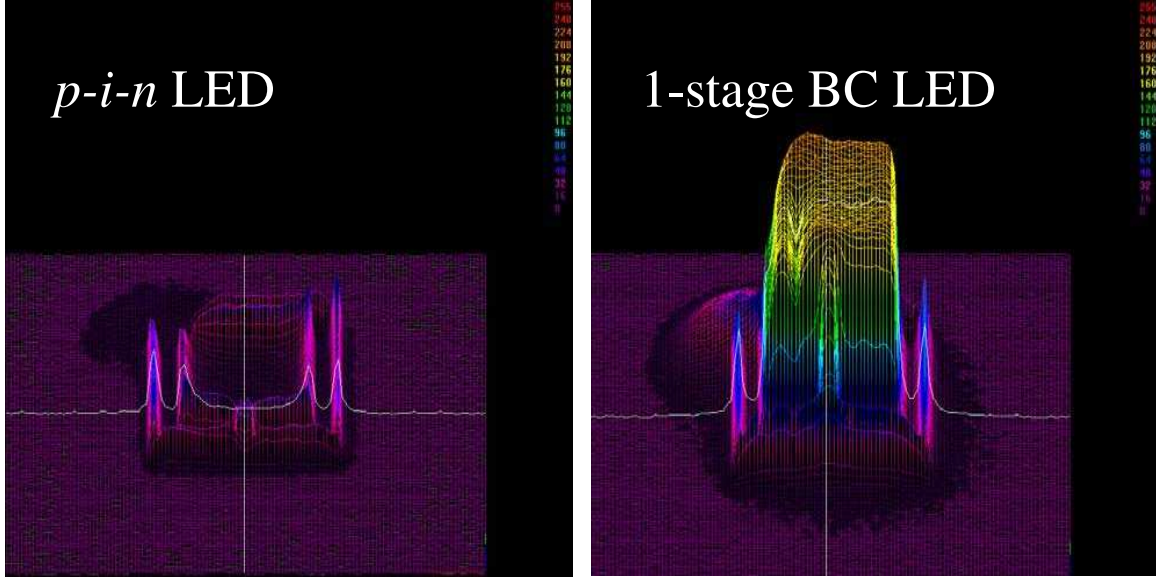
Figure 2.13:   Near-field intensity image of a 50 μm $\times$ 50 μm square mesa *p-i-n* LED (left) and a 1-stage BC LED with an n-doped OA layer (right) at a current injection of 50 mA. The camera intensity scale is identical for both devices.

the n-cladding and highly doped n-layer of the TJ then uniformly tunneling to efficiently provide holes into the valence band of the QWs.

Figure 2.14 shows luminescence uniformity for a) the *p-i-n* LED, b) 1-, c) 2-, d) 3-, and e) 4-stage BC LEDs with n-doped OAs at an operating current of 50 mA under identical image capture conditions. In all BC structures the uniformity is very consistent. The 4-stage BC LED shows the reduction of light output due to heating and the large power consumption.

This research shows that doping the graded intracavity OA layers of BC LEDs significantly improves device performance by reducing the required voltage, increasing optical recombination, reducing the red shift due to device heating, and increasing the saturation current where thermal rollover becomes evident. The TJs also improve light output from a given device, primarily by improving the current injection uniformity over the entire aperture of the device.

Clearly, the best choice of design amongst the four LED structures studied (*p-i-n*, undoped OA BC LED, n-doped OA BC LED, and p-doped OA BC LED) is the p-doped OA
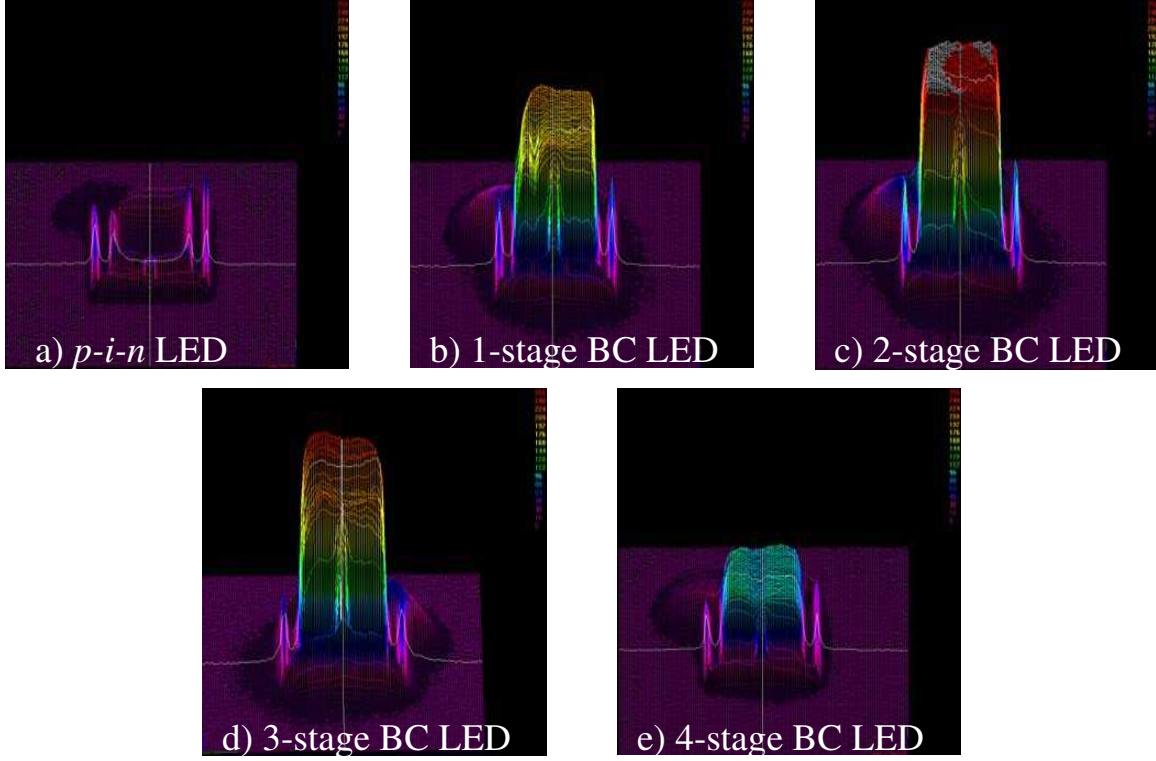
Figure 2.14: Near-field intensity images of 50 μm $\times$ 50 μm square mesa LEDs with n-doped OAs. a) *p-i-n* LED, b) 1-stage BC LED, c) 2-stage BC LED, d) 3-stage BC LED, and e) 4-stage BC LED, operating at a current injection of 50 mA. The camera intensity scale is identical for all devices.

BC LED. Both doped OAs BC LEDs significantly outperform the undoped OA BC LED. However, the p-doped OA BC LED has a significantly larger light output as compared to the n-doped OA BC LED. While the results for the BC LEDs point to the p-doped OA as the best device, this does not take into consideration of the cavity effects when incorporated into a VCSEL structure. Crosslight software capable of modeling the BC VCSEL structures was not able to be purchased due to the significant investment required. Therefore, with the results of the BC LED modeling and experimental data, the p-doped OA structure was chosen as the best structure for incorporation into the BC VCSELs for growth, fabrication, and characterization.

2.5 Bipolar Cascade Vertical Cavity Surface Emitting Lasers

2.5.1 Introduction. BC VCSELs are promising for producing signal gain under high-speed modulation conditions in the RF range [20]. A particular application of interest is that of RF-photonic links. BC VCSELs responsive to GHz injected current modulations can be used as the direct-drive optical signal generation device in such systems, greatly simplifying the component requirements and avoiding the insertion losses associated with external modulators. The central feature of BC devices is the use of reverse-biased TJs to efficiently source electron and hole currents to multiple active regions by recycling the valence band electrons resulting from optical recombination. Benefits of BC designs over typical *p-i-n* diode lasers include greater slope efficiency, and quantum efficiencies that can exceed unity when using multiple stages [11], improved RF impedance matching through increased series resistance [7], and reduced noise figures as a result of uncorrelated carrier recycling among stages [16].

Even though high-frequency performance is crucial, few reports of measured BC laser modulation data exist. Despite significant advances in InP- and GaAs-based BC VCSEL structures and their extensive characterizations [9, 14, 22, 34], to date we have located only the high-frequency analysis reported by Knödl, *et al.* [12] wherein modulated current efficiency factors are extracted from relative intensity noise measurements as a means of high-frequency characterization.

High-frequency measurements of modulated laser light output as a function of RF small-signal injected current for a series of BC VCSELs have been accomplished and reported [24, 26, 28]. The details of the growth and fabrication of GaAs-based BC VCSELs with operating wavelengths ~ 980 nm are presented. Measured BC VCSEL characteristics including LI, VI, and light power vs. drive power (LD), and small-signal laser modulation results approaching 10 GHz as a function of temperature are presented and discussed. For LD characterization, the drive power is defined as the device current multiplied by the applied voltage.

2.5.2 Bipolar Cascade Vertical-Cavity Surface-Emitting Laser Growth & Fabrication. Figure 2.15 a) illustrates the schematic layer diagram for a single-stage BC VCSEL structure, Figure 2.15 b) is a micrograph of a fabricated high-speed BC VCSEL device, and Figure 2.15 c) is a close-up scanning electron microscope (SEM) image of the BC VCSEL aperture. The BC VCSELs were grown on n^+ GaAs substrates by MBE. The laser cavities consist of 1-, 2-, or 3-stage $\frac{5}{2}\lambda$ microcavities, each containing a graded p-doped $Al_{0.98}Ga_{0.02}As$ OA [27] and a GaAs TJ [25] positioned at longitudinal nodes of the optical standing wave, and a triple QW active region placed at an antinode.
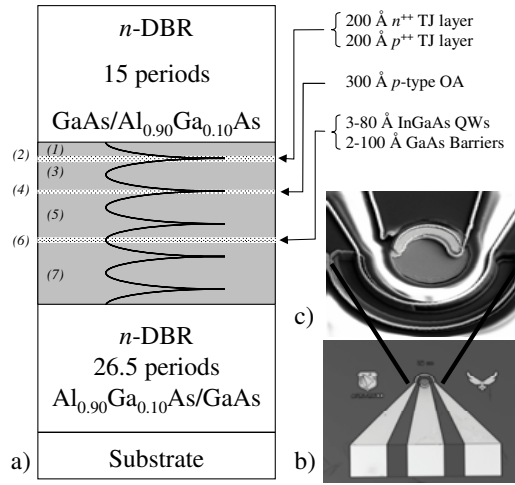
Figure 2.15: a) Schematic layer diagram of a single-stage BC VCSEL. The curve indicates the optical field of the $\frac{5}{2}\lambda$ cavity resonance. The insets show b) a micrograph of a processed high-speed device and c) a close-up SEM image of the VCSEL aperture.

The following description gives the layer structure for a 1-stage device. The top DBR consists of 15 abrupt $GaAs/Al_{0.90}Ga_{0.10}As$ pairs, Si-doped at 4×10^{18} cm^{-3}, each $\frac{\lambda}{4}$ thick. The microcavity is formed from the top DBR as follows (numbering scheme is indicated in Figure 2.15 a). First, an undoped GaAs spacer layer *(1)* is used to center a TJ *(2)* at the first node. The TJ is composed of a Si δ-doped GaAs layer with an effective doping level of 2×10^{19} cm^{-3} and a C-doped GaAs layer (doped at 1×10^{20} cm^{-3}); each TJ layer is 200 Å thick. Below this, an undoped GaAs spacer layer *(3)* positions an OA region *(4)* at the next node of the standing wave. The 300 Å thick OA is p-type $Al_{0.98}Ga_{0.02}As$ and has graded transition layers on either side. Under the OA is an approximately $\frac{3}{4}\lambda$ thick undoped GaAs

spacer layer *(5)* designed to place the active region in an antinode. The active region *(6)* consists of three 80 Å thick $In_{0.20}Ga_{0.80}As$ wells separated by 100 Å thick GaAs barriers. Finally, an undoped GaAs layer *(7)* approximately 1-λ thick is used to complete the cavity. For 2- and 3-stage structures, the entire microcavity is repeated. The bottom DBR consists of 26.5 abrupt $Al_{0.90}Ga_{0.10}As$/GaAs pairs with the same layer thicknesses and doping as the top DBR.

Top-contacted, mesa-isolated BC VCSELs with circular mesas varying from 10 to 50 μm in diameter were fabricated. Semi-ring annuli ohmic top contacts were formed lithographically and contact metal (50 Å Ni / 170 Å Ge / 330 Å Au / 150 Å Ni / 3,000 Å Au) was evaporated onto the patterned topside. The mesa dry etch was stopped on the third GaAs layer of the bottom DBR, just below the cavity as determined by in-situ reflectivity. The bottom contact was patterned and the same metals were deposited on both the patterned side and the backside (for thermal contact). The contacts were annealed in forming gas at 410 °C for 15 s. This annealing step was performed to allow for preoxidation device characterization. The OAs were formed with an in-situ oxidation furnace [6] at 400 °C for four hours, yielding an approximate 10 μm oxide penetration depth. The anneal and subsequent oxidation did not affect the quality of the ohmic contacts. Next, a 5,000 Å thick Si_3N_4 layer was deposited for electrical isolation and sidewall passivation, followed by a 5 μm layer of SU-8 (a very thick epoxy-based negative photoresist) used for planarization. The mesas and bottom contacts were opened lithographically and the uncovered Si_3N_4 was subsequently dry etched with Freon 23-O_2 (40 sccm-2 sccm) to completely clear out the mesa aperture and the electrical contacts. The ground-signal-ground *(g-s-g)* cascade contact pads were lithographically defined and Ti - Au (200 Å - 4,000 Å) layers were sputter deposited to ensure step coverage.

2.5.3   Bipolar Cascade Vertical-Cavity Surface-Emitting Laser Characterization.
The BC VCSELs were characterized to determine standard operating characteristics, as well as their high-speed performance. CW LI, VI and LD characteristics for 1-, 2-, and 3-stage BC VCSEL devices were measured at temperatures of -50 °C, -25 °C, 0 °C, and

+25 °C. The BC VCSEL characterization used the same system as for the BC LED characterization, discussed in Section 2.4.3, except a 5% neutral density (ND) filter was included to keep from saturating the photodetector.

Pulsed LI, LD, and VI characterization was not able to be performed on the BC VCSELs. While the AFRL Sensors Directorate has pulsed laser characterization capability for edge emitting lasers, the detector head cannot fit into the probe station's environmental chamber. Pulsed laser characterization would have provided valuable laser operating characteristics while neglecting the CW heating effects.

Table 2.3 details the complete characterization matrix for all temperatures, device mesa sizes, and number of stages. Laser characterization data was collected if the device lased, indicated by an "L" in Table 2.3, otherwise no data was collected and those devices were ignored for the remainder of the research. Frequency response measurements, indicated by an "F" in Table 2.3, were performed on lasing devices with mesa diameters up to 40 μm in diameter. The larger devices were ignored because of significant multimode operation. For smaller devices, frequency response measurements were not acquired either due to device failure while operating at a constant bias during the measurement or the frequency response was insignificant, $i.e.$, less than 2.5 GHz with a steady -20 dB per decade decay rate. Analysis of the BC VCSELs was performed as a function of number of stages and as a function of temperature.

High-frequency laser modulation response measurements were performed at the same temperature at 1 or 0.5 mA intervals along the positive slope of the LI curves. The output modulation was determined using the s-parameters obtained from an HP-8720A microwave network analyzer (MNA) [30] [8]. The test system consists of a stable CW current source connected to the Port-1 bias-tee of the MNA. The MNA applies a -10 dBm (0.1 mW) small-signal modulation onto the laser bias. The signal was supplied to the VCSEL by a 40 GHz coaxial microwave cable connected to the microprobe. The modulated light output was collected using a 63 μm core multimode fiber and detected using a 25 GHz high-speed detector. The output signal from the detector was returned to port 2 of the MNA via a 40 GHz

28

Table 2.3: Complete BC VCSEL characterization matrix. Collected laser characterization is indicated by an L and collected frequency response characterization is indicated by an F.

T (°C)	Mesa (μm)	1-Stage	2-Stage	3-stage
-50	20	L F		
	22	L F	L	L
	24	L F	L F	L F
	26	L F	L F	L F
	28	L	L F	L F
	30		L F	L F
	35		L F	L F
	40		L F	L F
	45		L	L
	50		L	L
-25	20	L	L	
	22		L	L
	24		L F	L F
	26		L F	L F
	28		L F	L F
	30		L F	L F
	35		L F	L F
	40		L	L F
	45			L
	50			L
00	22		L	L
	24		L F	L F
	26		L F	L F
	28		L F	L F
	30		L	L F
	35			L F
	40			L F
	45			L
+25	22			L
	24			L F
	26			L F
	28			L F
	30			L

microwave cable. The s_{21} and s_{11} parameters were measured by the MNA which was 2-port calibrated from 0.15 GHz to 20 GHz in 0.05 GHz steps and averaged ten times.

In order to compare independent measurements to a common -3 dB standard, the measured and fit frequency responses have been scaled by plotting

$$Response = 20log\frac{|s_{21}| \ or \ |MTF(\omega)|}{|MTF(0)|} \tag{2.1}$$

where MTF is the two-pole modulation transfer function. The two-pole form takes into consideration the low-frequency parasitic peak that was often observed. The scaling has been changed from 10log, as in reference [24], to 20log because the power was measured instead of the field resulting in the square term coming out of the logarithm. This kept the measured -3 dB frequency response at or below the calculated maximum frequency response extracted by the K-factor, to be described later in this section. Unfortunately, the maximum -3 dB frequency response was reduced from 9.3 GHz to 7.1 GHz for the best performing devices.

The functional form for the two-pole MTF fitting function was derived to be

$$|MTF(\omega)| = \sqrt{\frac{A + B + C}{(1 + \tau_{par}^2\omega^2)[\gamma^2\omega^2 + (\omega^2 - \omega_r^2)^2]}} \tag{2.2}$$

where the independent variable ω is the angular frequency and

$$A = C_m^2(1 + \tau_{par}^2\omega^2)\omega_r^4 \tag{2.3}$$

$$B = 2C_mC_{par}\omega_r^2[(\gamma\tau_{par} - 1)\omega^2 + \omega_r^2] \tag{2.4}$$

$$C = C_{par}^2[\gamma^2\omega^2 + (\omega^2 - \omega_r^2)^2]. \tag{2.5}$$

The fit parameters include: $\omega_r = 2\pi f_r$, the relaxation oscillation frequency; γ, the damping rate; C_m, the single pole MTF amplitude constant; C_{par}, the parasitic amplitude constant; and τ_{par}, the parasitic time constant which is converted to a parasitic frequency, f_{par} by

$$f_{par} = \frac{1}{\tau_{par}}. \tag{2.6}$$

With these fit parameters, other important parameters [4] such as the peak frequency, f_{peak},

$$f_{peak} = \sqrt{f_r^2 - \frac{\gamma^2}{8\pi^2}} \tag{2.7}$$

and the calculated -3 dB frequency, $f_{-3\ dB\ Calc}$,

$$f_{-3\ dB\ Calc} = f_{peak}^2 + \sqrt{f_{peak}^4 + f_r^4} \tag{2.8}$$

are determined. These fitted and calculated parameters were obtained for all frequency response measurements as a function of bias current.

The damping rate is proportional to the square of the relaxation oscillation frequency [1, 3, 4, 10]

$$\gamma = K f_r^2 + \frac{1}{\chi\tau_n} \tag{2.9}$$

where τ_n is the differential carrier lifetime and χ is a factor accounting for carrier transport effects. This K-factor is used to estimate the maximum intrinsic modulation bandwidth when only considering the damping rate by [1, 3, 4, 10]

$$f_{-3dB\ damp} = \frac{2\sqrt{2}\pi}{K}. \tag{2.10}$$

Similarly, the thermally-limited modulation bandwidth is given by [1, 10]

$$f_{-3dB\ therm} = \sqrt{1 + \sqrt{2}} f_{r\ max} \tag{2.11}$$

and the modulation bandwidth limited by parasitics is [1, 10]

31

$$f_{-3dB\ par} = (2 + \sqrt{3})f_{par}. \tag{2.12}$$

Figure 2.16 shows a representative set of measured and fit frequency response data for the 28 μm mesa device at a mount temperature of -50 °C. The frequency response for this device was performed with 1 mA steps from 2 to 12 mA. Figure 2.16 shows current steps from 2 to 6 mA to illustrate the frequency response with respect to injected current.
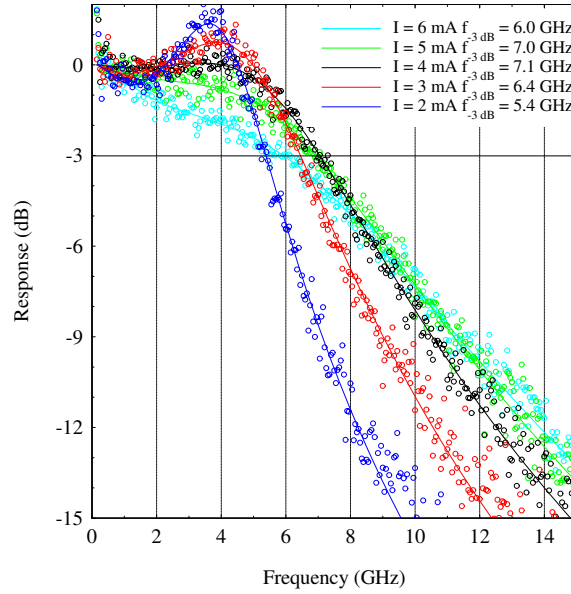
Figure 2.16:   Measured and fit frequency responses for 28 μm diameter mesa 3-stage BC VCSELs at a mount temperature of -50 °C. Current steps of 1 mA were performed from 2 mA to 12 mA, but only the 2 through 6 mA data and fits are shown to detail the relation as a function of CW drive current.

2.5.3.1   Standard Laser Characterization Results (LI, LD, and VI).   Figure 2.17 shows the operating characteristics for 1-, 2-, and 3-stage BC VCSELs with 28 μm mesas at a chuck temperature of -50 °C. The operating characteristics include CW a) LI, b) LD, c) VI, and d) frequency response characteristics. This mesa and temperature combination represents the overall best performing single-mode light power and frequency response for both the 2- and 3-stage BC VCSELs. The 1-stage devices lased at -50 °C but not at other temperatures due to low gain resulting from cavity detuning relative to the gain peak and from small round-trip gain due to the low number of DBR pairs and only three QWs. This

32

detuning results in degraded CW performance of all of the BC VCSELs at higher tempera-
tures. The VI data in Figure 2.17 c) unequivocally shows the expected BC VCSEL behavior
as the number of stages is increased.
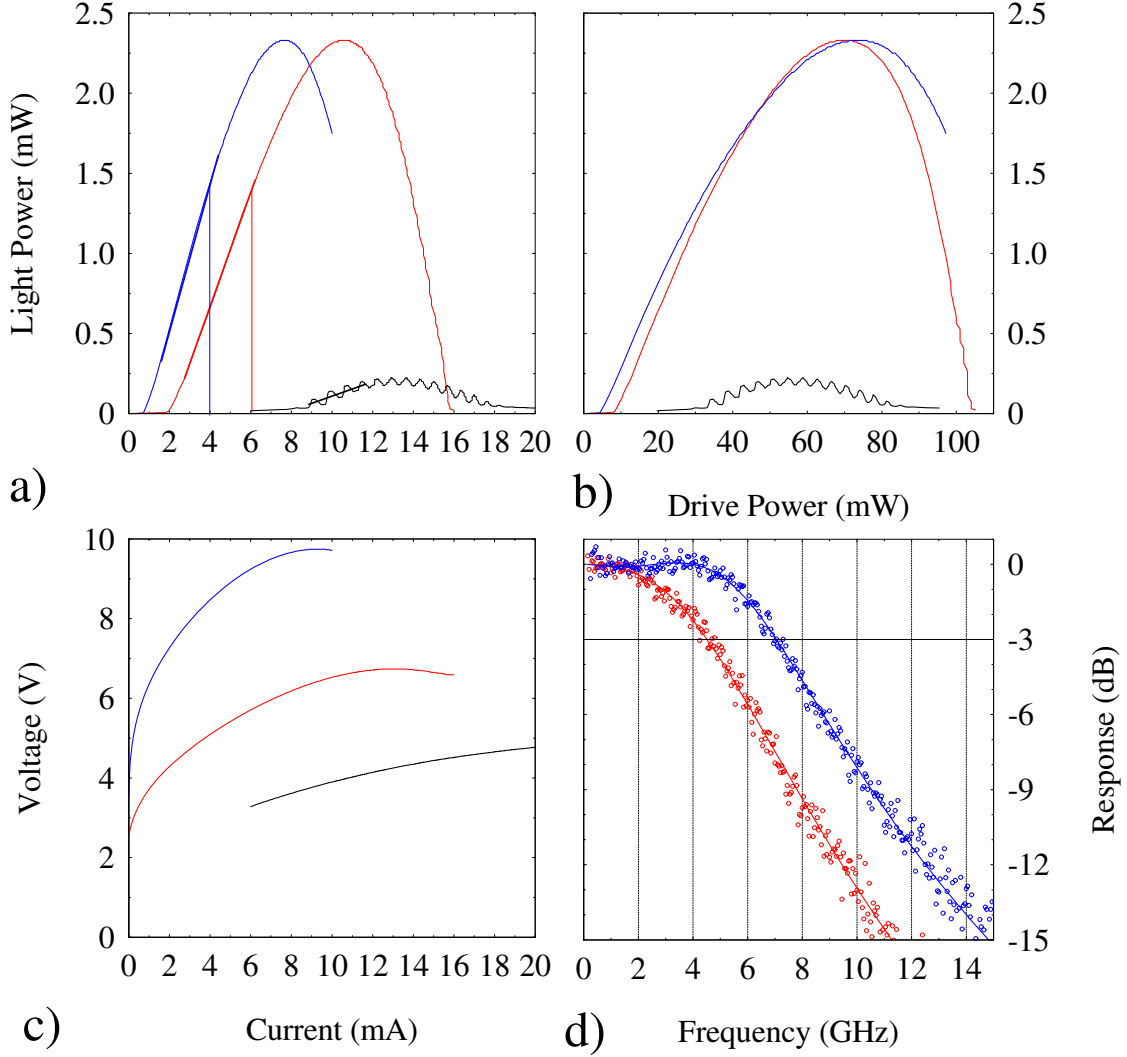
Figure 2.17:   Operating characteristics for 28 μm mesa 1- (black), 2- (red), and 3-stage
(blue) BC VCSELs at a mount temperature of -50 °C. a) is the LI, b) is the LD, c) is the
VI, and d) is the frequency response. The heavy line portions of the LI curves indicate the
linear regime where the slope efficiencies were calculated. The vertical lines in a) are the
currents where the frequency response characterization was obtained.

Several mesa diameters lased at all of the temperatures of characterization for the
3-stage BC VCSEL. The best operation in all cases was at -50 °C, but mesas ranging from
22 μm to 30 μm in diameter also lased at room temperature. The most complete set of data

occurred for the 3-stage BC VCSEL with mesa diameter of 28 μm, where a complete set of LI, LD, VI, and frequency response characteristics was made over all of the temperatures listed.

The "electron recycling" benefit of the BC VCSEL structure is immediately obvious by comparing the 2- and 3-stage LI and LD data in Figures 2.17 a) and b). The increased round trip gain from the additional stage manifests in a rise in slope efficiency, η_{slope}, from 0.36 W/A for the 2-stage device to 0.46 W/A for the 3-stage device, as well as the reduction in the threshold current from 2.0 mA for the 2-stage device to 0.7 mA for the 3-stage device. Again, the 1-stage LI and LD results are significantly reduced, because of the reasons stated above, with a slope efficiency of 0.05 W/A and a threshold current of 8.0 mA.

An important observation is seen in Figure 2.17 b). It has been repeatedly emphasized in the literature that BC structures do not make light for free. As the number of stages is increased, there will be a corresponding increase in voltage. However, increasing the number of stages reduces the threshold and operating currents and, for the same drive power, the same amount or more light power is generated with additional stages. BC VCSELs improve slope efficiency and improves wall-plug efficiency, $\eta_{wallplug}$!

As mentioned previously, the 1-stage BC VCSEL did not perform nearly as well as the 2- and 3-stage BC VCSELs due to the low number of DBR mirror pairs reducing the round trip gain in a 1-stage device, thereby requiring the device to be driven harder to achieve threshold and developing undesired heating effects. These heating effects are responsible for the "ripple effect" observed in the LI, Figure 2.17 a), and LD, Figure 2.17 b), characterization [4]. The low-current truncation in the 1-stage LI, LD, and VI is due to the limited data range of the HP-7145A SPA. A maximum of 256 data steps was available, limiting the current step size or current range. Several devices had this problem, where truncation was required to scan the full lasing range with a current step size small enough to avoid destroying the device being tested.

Figure 2.18 shows the operating characteristics for the 3-stage BC VCSEL with a 28 μm mesa at chuck temperatures of -50 °C, -25 °C, 0 °C, and 25 °C. The operating

characteristics include CW a) LI, b) LD, c) VI, and d) frequency response. One can observe that the light power drops off by nearly an order of magnitude from -50 °C to 25 °C. Another observation is the nearly linear translation of the light peak power with increasing drive current, Figure 2.18 a) or power, Figure 2.18 b). This is the key indicator that the InGaAs QW gain peak is poorly aligned with the cavity resonance for room temperature operation. By judiciously reducing the well width, the alignment of the QW gain peak and cavity resonance can be optimized for room temperature operation. Figure 2.18 c) also shows the expected reduction in voltage with increasing temperature due to bandgap narrowing as the temperature increases.

Table 2.4 summarizes several important parameters for these 28 μm devices, including threshold current (I_{th}), slope efficiency (η_{slope}), wall-plug efficiency, ($\eta_{wallplug}$), frequency response drive current ($I_{freq\ resp}$), and -3 dB frequency ($f_{-3\ dB\ Meas}$).

Table 2.4:   28 μm diameter mesa BC VCSEL operating parameters.

Temp. °C	Stage	I_{th} (mA)	η_{slope} (W/A)	$\eta_{wallplug}$ (W_{opt}/W_{elec})	$I_{freq\ resp}$ (mA)	$f_{-3\ dB\ Meas}$ (GHz)
-50	3	0.7	0.46	0.05	4.0	7.1
	2	2.0	0.36	0.05	6.0	4.5
	1	8.0	0.05	0.01		
-25	3	0.7	0.39	0.05	4.0	6.5
	2	1.8	0.28	0.05	4.5	4.3
00	3	0.9	0.32	0.04	3.0	5.3
	2	3.0	0.10	0.02	5.0	2.2
+25	3	1.8	0.13	0.02	3.5	3.4

2.5.3.2   High-Speed Laser Characterization Results.   Figure 2.17 d) shows the frequency response for the 3- and 2-stage 28 μm diameter mesa devices at the chuck temperature of -50 °C/ [24]. These are the first reported results for BC VCSELs. The 3- and 2-stage BC VCSEL devices exhibit -3 dB frequency responses of 7.1 GHz and 4.5 GHz, respectively, at the labeled biasing conditions. The 3-stage device at +25 °C, shown in Figure 2.18 d), does operate under small-signal modulation with a 3.4 GHz -3 dB response cutoff. However, the modulation peak is quite sharp, indicating increasing the current injection should increase the -3 dB frequency bandwidth. Unfortunately, the modulation signal
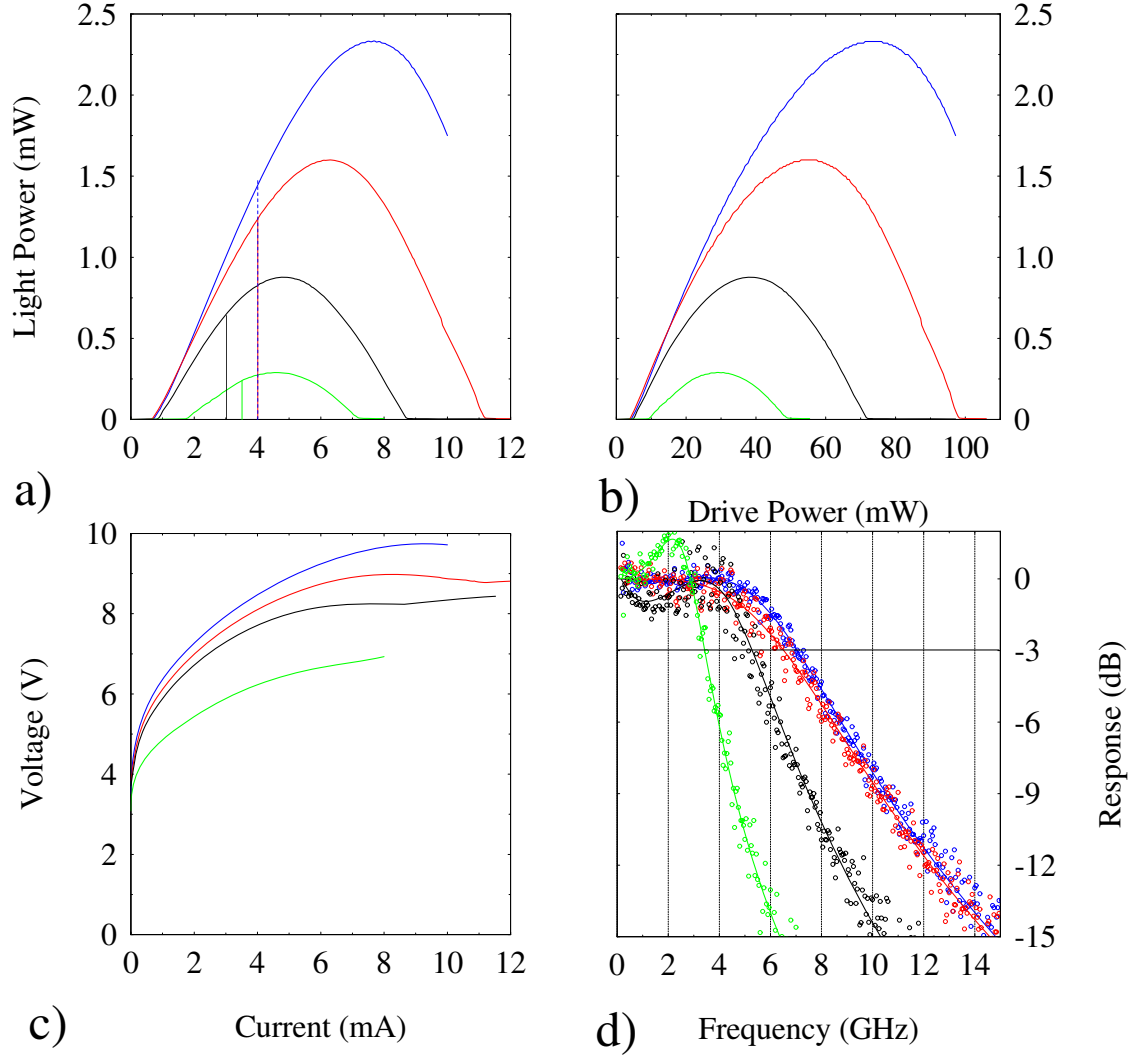
Figure 2.18: Operating characteristics for 28 μm diameter mesa 3-stage BC VCSELs at mount temperatures of -50 °C (blue), -25 °C (red), 00 °C (black), and +25 °C (green). a) is the LI, b) is the LD, c) is the VI, and d) is the frequency response. The vertical lines in a) are the currents where the best frequency response characterization was obtained.

falls off at higher bias currents because the laser is operating near the maximum of its positive LI slope, $i.e$ the gain peak is red-shifting out of the cavity resonance. Increasing the current reduces the -3 dB frequency response as the laser operation begins to degrade due to heating effects and increasing gain-cavity mismatch.

The MTF curves for the devices in Figure 2.17 d) correspond to fits with relaxation oscillation frequencies of, $f_r \equiv \omega_r/2\pi =$, 4.78 and 6.27 GHz, and damping rates of, $\gamma =$,

35.4 and 46.3 ns^{-1} for the 2-stage and 3-stage measurements, respectively. Figures 2.19 a) and b) show the damping rate, γ, as a function of resonance frequency squared, f_r^2 for the 3- and 2-stage BC VCSELs, respectively, with 28 μm diameter mesas, as well as the associated K-factor. Figures 2.19 c) and d) show the calculated -3 db frequency, measured -3 db frequency, relaxation oscillation frequency, and peak frequency as a function of $(I - I_{th})^{1/2}$ for the same 3- and 2-stage BC VCSELs, respectively. It is apparent that thermal saturation is an issue with these devices. The roll-off of the peak frequency, f_{peak}, indicates a strong thermal limit to the frequency response along with the strong damping limitation. Parasitic limitations do not appear to be an issue, indicating device design improvements such as (1) improving the room-temperature resonant cavity-InGaAs QW gain peak alignment and (2) grading the DBR mirrors will significantly improve device performance by improving the thermal characteristics of the devices.

Table 2.5 summarizes the high-speed parameters for the 3- and 2-stage BC VCSELs studied in detail and includes a comparison to a SOA room temperature operating 840 nm VCSEL with a 6 μm OA [1]. Since this is the first reported frequency modulation of BC VCSELs there are no BC VCSEL values to compare with. However, a useful comparison with a SOA high-speed semiconductor laser will provide a useful comparison. The K-factor for the BC VCSELs is extremely large (more than 3$\times$) compared to the 840 nm VCSEL. This is the primary parameter that must be reduced because it leads directly to a large $f_{-3dBdamp}$ and $f_{-3dbtherm}$.

2.6 Summary

The design and demonstration of 1-, 2-, and 3-stage BC LEDs and VCSELs has been accomplished. The BC LEDs provided unique information on the best layer structure to use in the microcavity of a BC VCSEL. The BC VCSELs all operated at -50 °C and exhibited the first reported frequency response characterization for and type of BCL. The 3-stage BC VCSEL did operate at room temperature. These results show that a BC VCSEL will operate at high-speeds and with high slope efficiencies which are required for an RF photonic link. However, further improvements are required to optimize the BC VCSEL for
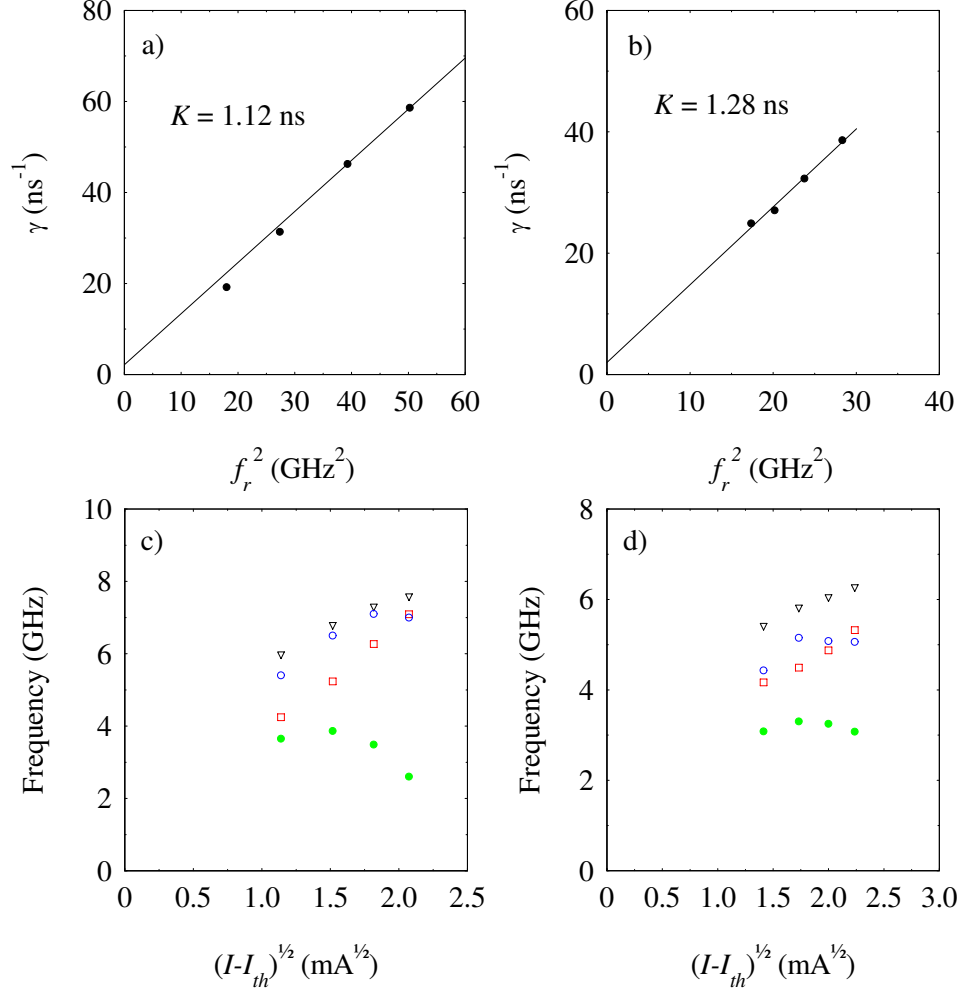
Figure 2.19:   High-frequency parameter analysis for 2- and 3-stage BC VCSELs at a mount temperature of -50 °C. a) and b) shows the damping rate, γ, as a function of resonance frequency squared, f_r^2 for the 3- and 2-stage, respectively, BC VCSELs with 28 μm diameter mesas as well as the associated K factor. c) and d) shows the calculated -3 db frequency (black triangles), measured -3 db frequency (blue circles), fitted relaxation oscillation frequency (red squares) and calculated peak frequency (green dot) as a function of $(I - I_{th})^{1/2}$ for the same 3- and 2-stage, respectively, BC VCSELs.

Table 2.5: Frequency modulation parameters for 3- and 2-stage BC VCSELs with 28 μm diameter mesas at -50 °C and a comparison to a state-of-the-art 840 nm VCSEL with a 6 μm aperture operating at room temperature [1].

Parameter	Units	3-Stage BC VCSEL	2-Stage BC VCSEL	840 nm VCSEL
I_{bias}	mA	4	6	4
f_r	GHz	6.27	4.88	9.5
γ	ns^{-1}	46.3	35.4	$\sim$45
$f_{-3\ dB\ Calc}$	GHz	7.30	6.05	8.3
$f_{-3\ dB\ Meas}$	GHz	7.10	5.08	$\sim$8
f_{peak}	GHz	3.49	3.25	6.5
f_{par}	GHz	5.14	8.08	n/a
K	ns	1.12	1.28	0.40
$f_{r\ max}$	GHz	7.10	5.33	9.5
$f_{-3\ dB\ damp}$	GHz	7.93	6.94	22
$f_{-3\ dB\ therm}$	GHz	11.0	8.28	14.7
$f_{-3\ dB\ par}$	GHz	19.2	30.2	24

room temperature operation. First and foremost, the QW gain peak and the cavity resonance has to be better aligned. Other improvements for increasing high-speed operation include DBR mirror pair optimization for the stage to be studied and specially designed fabrication masks to minimize capacitance issues between mesa sizes and thickness differences due to the number of stages employed. All of these improvements will contribute to reducing the K-factor.

III. Bipolar Cascade Resonant Cavity Light Emitting Diode

3.1 Introduction

This chapter discusses the methodology used in developing the STRiped EMittER (STREMER). The STREMER is a BC resonant-cavity light emitting diode (RCLED), which is not a typical LED, but a collection of technologies that improve the operational output of the basic LED. For this reason, several preliminary experiments were necessary prior to settling on a final device design. The purpose of these preliminary experiments was to

- Determine the appropriate growth process for best TJ current vs voltage (I-V) slope under forward bias

    - An abrupt dopant profile is demanded for best TJ characteristic curve.

- Determine the optimal location of the TJ with respect to the ARs.

    - Highly doped TJ are scattering centers and heat sources and could reduce overall device power

- Determine the impact of heat on the resonance peak of the resonant cavity (RC)

    - RC will be designed with a red shifted center frequency in expectation of the red shifted emission spectrum from the InGaAs MQWs. This allows the emission peak to match the cavity resonant peak under normal operation.

Some features were also modeled using Crosslight® software, a finite element analysis tool for semiconductor device modeling. Crosslight is composed of a number of computer aided design simulation modules, which simulate the electronic and optoelectronic properties of semiconductor devices. The simulation packages are based on finite element analysis in two and three dimensions. There are a number of physical and numerical models utilized to calculate various parameters describing the performance of the device simulated.

The APSYS module, with the quantum mechanical tunneling capability, was used to model the behavior of wide area BC-RCLEDs. APSYS is a general-purpose two dimen-

sional finite element analysis and modeling software program, and was used to generate the following pertinent data:

- Current versus voltage characteristic

- Band diagrams under various bias conditions

- Spontaneous emission spectrum as a function of current

Because the preliminary testing was essential to developing the final design, a brief summary of the conclusions reached from each test is included. Tests include: 1) TJ growth process investigation, and 2) TJ-AR separation (TAS) determination, to establish an appropriate distance to insert between the TJ and AR to lessen the impact of the TJ on beam uniformity, total output, and wavelength shift.

3.2   Tunnel Junction Optimization

To produce an optimal BC device, a quality TJ is key. Once an optimal TJ growth process was identified, it could be integrated into the growth with the other device layers. Fabrication of RCLEDs has been perfected over many years and many standard growth processes exist and were used as a template for this device

3.2.1   Tunnel Junction Growth Process .   Six different TJ samples were used for this investigation. All samples were grown by molecular beam epitaxy in a Varian Gen-II system. The various test samples are shown in Table 3.1. The wafers were labeled G2-3255, G2-3256, G2-3257, G2-3258, G2-3259, and G2-3260. Wafers 3255 and 3256 are identical growth runs to test system variation.

To form the TJ, degenerately doped n-type and p-type epitaxial layers were grown on n-doped GaAs substrates at a temperature of 680 ^oC, which is a typical growth temperature for this structure. For high quality TJs (those with low resistivity) the *p-n* junction must have an extremely abrupt doping profile, creating a thin space charge region that will increase the probability of quantum mechanical tunneling [5]. Doping levels for the TJ layers are 1 x 10^{20} cm^{-3} for the Be doped p-layer and 8 x 10^{18} cm^{-3} for the Si doped n-layer. Si

Table 3.1: Device labeling and description of the growth processes, to include adding structures, or altering the vacuum gas flow, and the growth temperature.

Wafer Number	Growth Variation	Growth Temperature
G2-3255	Standard	575^oC
G2-3256	Standard	575^oC
G2-3257	30 sec As flow inserted	575^oC
G2-3258	20 Å smoothing layer inserted	575^oC
G2-3259	Remove 3.5 sec As flow after each δ-doped layer	680^oC
G2-3260	Remove 3.5 sec As flow, added 20 Å smoothing layer	680^oC

becomes amphoteric for dopant levels this large, if this is coupled with growths at high temperatures, a self-compensation of the doped layer can occur. To mitigate these issues, δ-doping was used to establish a high doping level throughout the n-layer. The growth of 10 Å δ-doped layers was repeated 20 times, resulting in a 200 Å n-doped layer. Also, it has been reported that reducing the substrate temperature below 400 °C controls the self-compensation effect [18], but because this layer is in the AR, it is preferable to grow it at the same temperature as the QWs.

Samples 3255 and 3256 were produced by growing the n^{++} layer directly on the p^{++} layer, resulting in the formation of the TJ. The next sample, 3257, has a 30 sec As flow inserted into the growth. The As overpressure step allows n dopant (Si) to clear out of the chamber reducing the possibility of self compensation in the p^{++} layer. Sample 3258 has a 20 Å undoped smoothing layer added to the structure, between the n and p regions, to enhance the abrupt junction. By adding the smoothing layer, fewer dopants from the degenerately doped n layer will diffuse into the degenerately doped p layer during growth. In the baseline samples as well as sample 3257, a 3.5 sec As flow is done after each 10 Å δ-doped layer is grown, but sample 3259 has these steps removed. The 3.5 sec As flow is done after each δ-doped layer to allow time for the dopants to diffuse into the layer. Lastly, sample 3260 has the 3.5 sec As flow removed and the 20 Å undoped smoothing layer added. These modifications were expected to increase the chances of the formation of an abrupt

TJ, thus reducing the size of the space charge region, which will reduce the resistance of the structure.

Another modification to the baseline growth process was to vary the growth temperature. Typically, GaAs structures are grown above 600 °C to produce high purity material, several of the growths were at 575 °C to reduce the likelihood of dopant diffusion from other layers. Only devices G2-3259 and G2-3260 were grown at the higher temperatures.

Electron beam (E-beam) evaporation was used to deposit 300 Å Ti, 500 Å Pt, and 3500 Å Au, which formed the top p-contact metal. The rear surface of the wafer was evaporated 50 Å Ni, 170 Å Ge, 330 Å Au, 150 Å Ni, 3000 Å Au, which formed the n-contact. These metal compositions are the standard metallizations used at AFRL/RY. Ti and Ni are used as seed layers for adhesion, Au/Ge is a widely used n-ohmic metal alloy, the Pt layer is used as a barrier layer to prevent electromigration, and the gold is the contact surface.

A Tektronix Curve Tracer was used to produce an I-V curve for each device tested from the respective wafer samples. The I-V curves were used to aid in understanding the impact of the variations made during the growth process. The curve tracer itself, produced a linear I-V curve when the probe was placed in direct contact with the curve tracer base. This linear curve is shown in Figure 3.1. This slope is a conductance, and by taking the reciprocal, the resistance of the apparatus, is found to be $R_{apparatus} = \Omega^{-1}$.

Processed and tested devices ranged in size from smallest to largest, $50 - 1600$ μm. The smallest devices were the most resistive, and least affected by the apparatus' resistance, while the largest ones (larger than 200 μm) were the least resistive and were greatly influenced by the curve tracer resistance. For this reason, only the 50 and 100 μm devices were analyzed for best TJ slope efficiency determination. Figure 3.2.1 shows I-V curves for all 50 μm devices tested. A quantitative comparison revealed that devices from wafer samples G2-3255 and G2-3258 showed the steepest slope, reflecting that these TJs had the highest probability of quantum mechanical tunneling at the lowest applied voltage. Figure 3.2.1 shows a plot of the measured I-V curve of a 50 μm device from wafer G2-3258, and

Characteristic I-V Curve for Curve Tracer
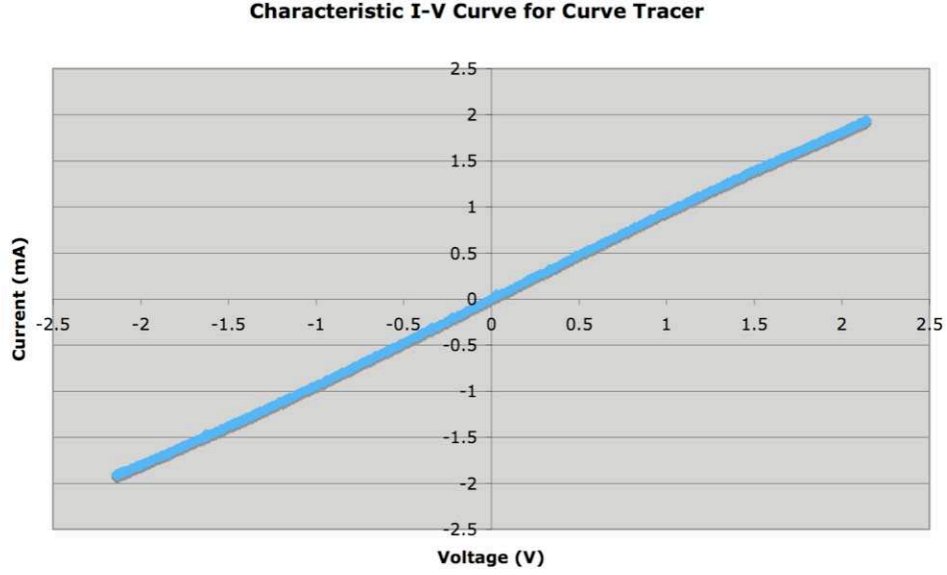
Figure 3.1:   The Tektronic curve tracer I-V curve. This linear I-V curve was produced by the curve tracer probe tip being placed in direct contact with the base.

Figure 3.4 provides a closer snapshot of the region of interest, curve-fitted, with the linear regression equation established. A slope of ~0.2 A/V was observed in the measured data.

These TJs were modeled with Crosslight and plots of the unbiased and biased energy bands are shown in Figure 3.5 and Figure 3.6. The green dotted line in the unbiased band diagram is the Fermi level, and the multiple green dotted lines in the biased band diagram are the quasi-Fermi levels that manifests under forward bias. The I-V curve of the modeled device is shown in Figure 3.7, and it has a slope of ~ 0.2 A/V as well.

Even though the curves do not look identical, the slope of the curve is the key for producing a model that is in close agreement with the measured values. Focusing on the voltage range from 0.0 to -0.8 V, the actual slope of the measured data is 0.1672 A/V, and the modeled data has an actual slope value of 0.1847 A/V. Again, each of these values are conductances, and by taking the reciprocal, the resistance is found. Therefore the measured resistance $R_{measured} = 1/0.1672 = 5.98$ Ω, and the modeled resistance $R_{modeled} = 1/0.1847 = 5.414$ Ω. Since the measured data was influenced by the curve tracer's resistance, $R_{apparatus}$ must be subtracted from $R_{measured}$, leaving the actual mea-

44
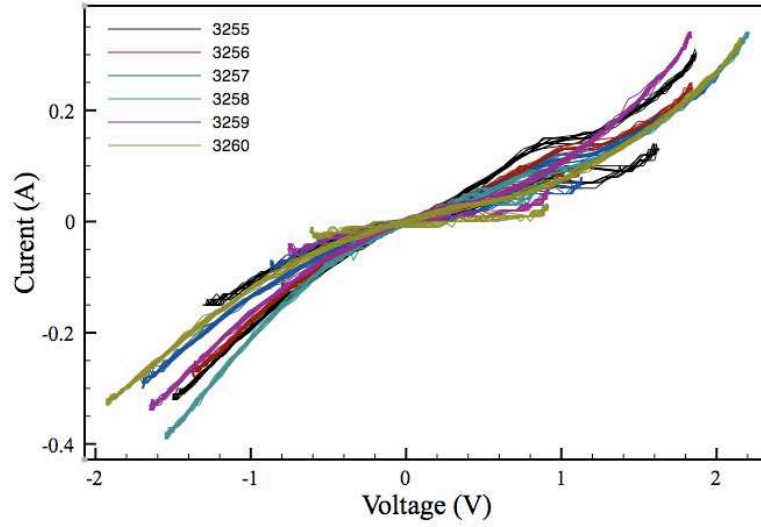
Figure 3.2:   Measured I-V curves taken from all 50 μm devices tested. Devices from wafer samples G2-3255 and G2-3258 show the best slope efficiency.
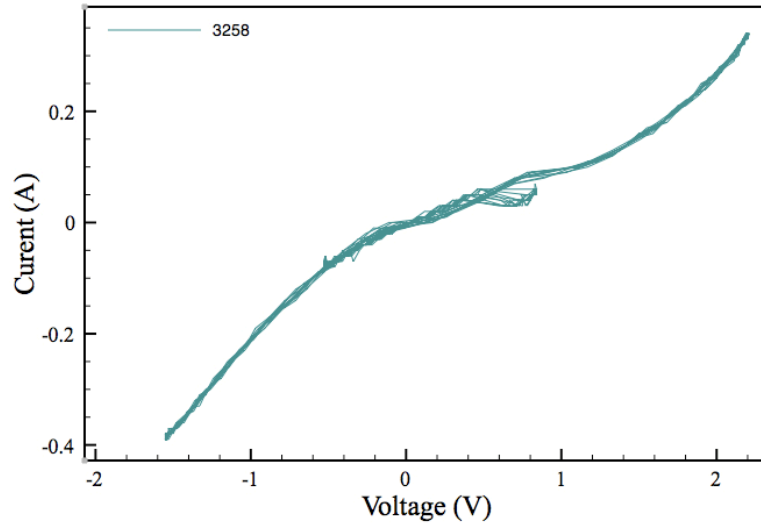
Figure 3.3:   Current-voltage characteristic recorded by the curve tracer. Focusing on the lower left portion of the curve, a slope of $\sim$ 0.2 A/V was calculated.
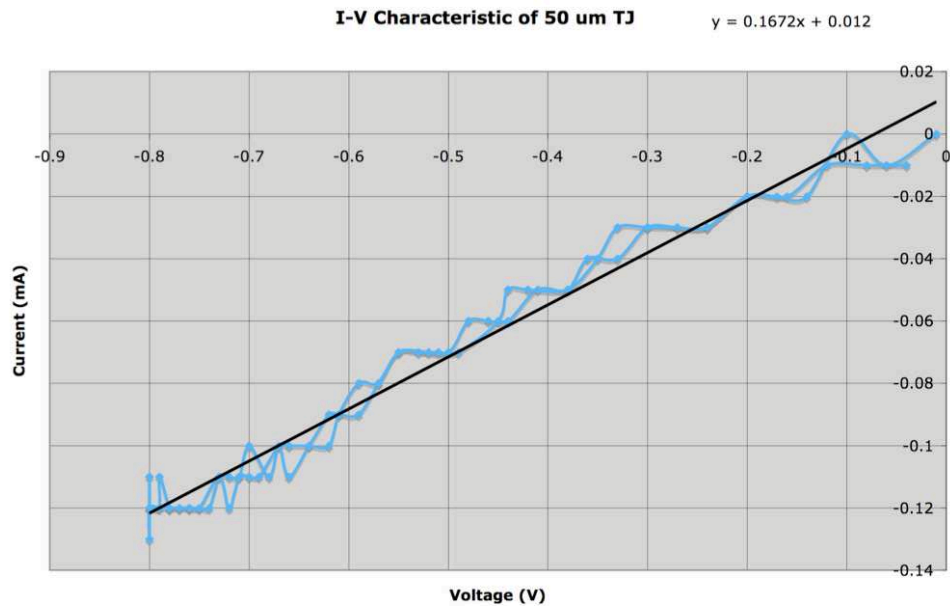
Figure 3.4:   A close up view of the lower left portion of the I-V curve of devices from G2-3256. A slope of ~ 0.2 A/V was calculated, and the steepest slope is most desirable. The multiple traces shown in the figure are a result of noise from the curve tracer.
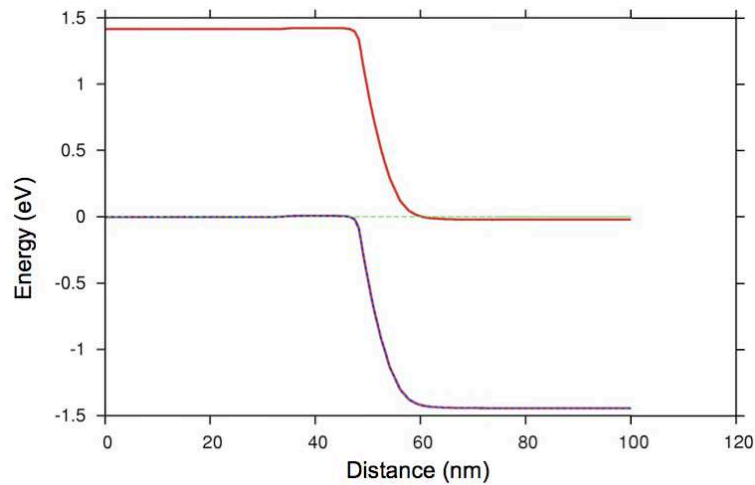
Figure 3.5:   The TJ under 0 V bias condition. The green dotted line is the Fermi level. Degenerate doping brings the conduction band and valence band into close proximity at the junction.

46
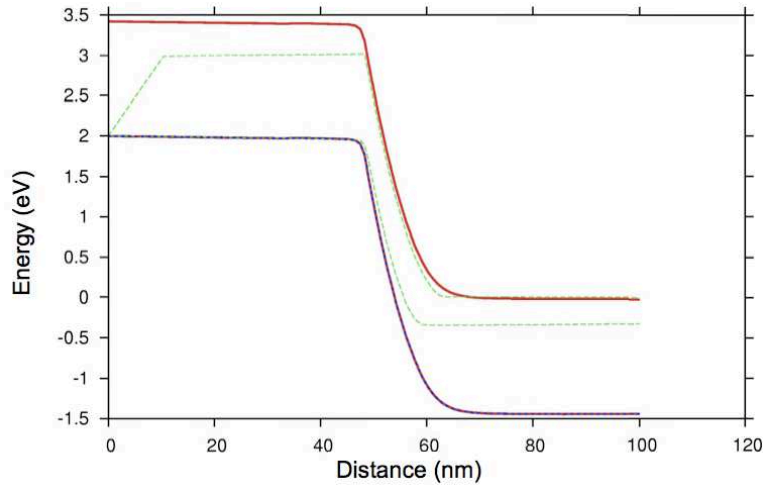
Figure 3.6: The TJ under forward bias condition. The green dotted lines are the quasi-Fermi levels. Under forward bias, the degenerate layers are separated by a thin forbidden energy gap, increasing the probability of electron tunneling.
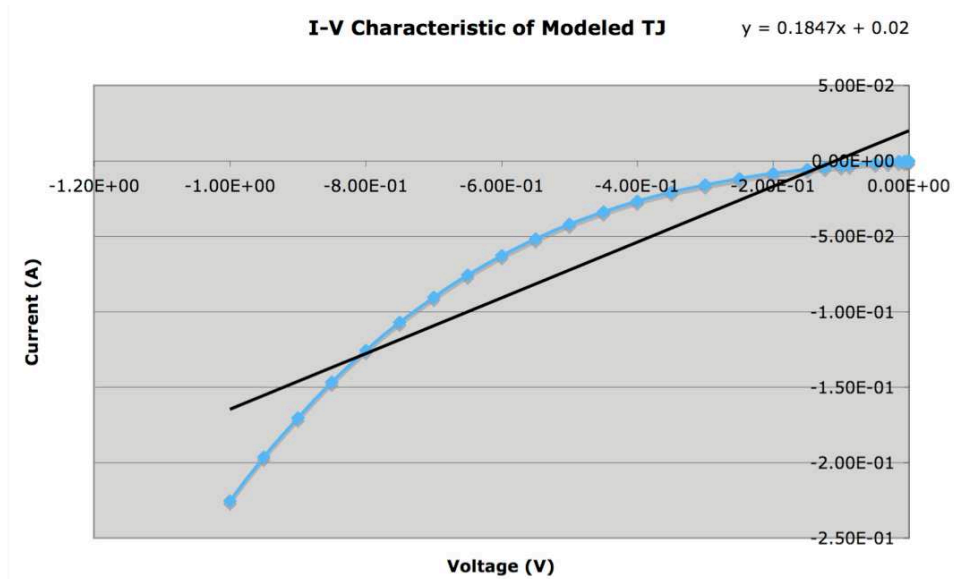
Figure 3.7: Current-voltage characteristic of TJ produced by Crosslight. The overall slope of this curve is ~ 0.2 A/V, showing good agreement with measured values.

sured resistance $R_{actual} = 4.98\ \Omega$. The difference between R_{actual} and $R_{modeled}$ is about 8%, which proved to be acceptable for this investigation from subsequent device modeling.

Although the TJs grown for this test are suitable for our application, this series of tests show that the lower temperature devices produce a better slope, under reverse bias, in all devices. From this data, it was determined that G2-3256 and G2-3258 possessed the steepest slope, 0.2 A/V. The TJ growth process used for wafer G2-3256 was selected for use in this application, since the only difference between the devices on the two wafers is that G2-3258 has a 20 Å smoothing layer between the p^{++}/n^{++} junction, suggesting a simpler growth process for G2-3256.

3.2.2 TJ-AR Separation Layer Thickness Optimization. Highly doped layers represent carrier traps in semiconductors, and doping increases the number of imperfections, which lead to an increased number of traps, within the material. An increase in the number of scattering centers increases the probability of Shockley, Reed, Hall (SRH) recombination occurring. It is possible that a large doping concentration induces an increased number of traps and these traps can reduce the total output power. Additionally, TJs are heat sources, since they are resistive to a degree, and temperature greatly impacts device operation, as discussed previously. Finally, the TJ will exhibit a fairly strong electric field that could impact carrier flow. For these reasons we must isolate the TJ and the AR by spacer layers. A TAS investigation was conducted to determine an optimum location for the TJ with respect to the AR, and determine the impact this separation has on device uniformity, the amount of thermally induced wavelength shift, and device total output power.

For these investigations, three different TAS distances were selected and are shown in Table 3.2. Each distance locates the TJ in a node within the RC. Figure 3.8 shows the layer structure, which includes, metal contacts, spacer layers, a MQW AR, the TAS layer, the TJ formed by degenerately doped n- and p-type layers and the GaAs substrate. Also, a set of DBR pairs form a cavity around the TJ and AR.

Data collection was done using a Cascade Microtech probe station with an IR camera mounted to a telescope to record the beam profile. An ILX Lightwave current supply was

48

Table 3.2:   The distance between the TJ and AR in the respective samples. The TAS layer is measured in Å.

Wafer	TAS (Å)	Wafer Number
1	3045.0	G2-3263
2	1742.5	G2-3262
3	250.4	G2-3261
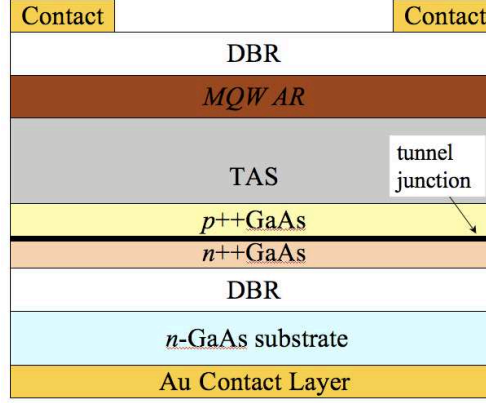
Figure 3.8:   Device layer structure showing the TAS layer in the device. The TAS layer thickness is varied to move the TJ away from the AR.

used to power the devices. In each device, the TJ was placed in a node to minimize carriers from being scattered by the TJ. All devices were 300 μm in diameter with a 5 μm wide metal contact ring on the surface, with a 30 μm section of the contact used for probing. The total cavity thickness of all of the devices used was $4\lambda/2$, or 5568 Å, with $\lambda = 980$ nm and $n_{GaAs} = 3.5$.

Additional devices were fabricated with sizes varying from 80 μm to 200 μm, to identify the limit to the effectiveness of the TJ as a current spreading layer in these devices. All of these additional devices were one stage BCLEDs with 25 μm metal contact layers.

3.2.2.1   TAS Layer Thickness vs Uniformity .   From previous assessments, the TJ was expected to improve uniformity across the surface of wide area devices over that of the standard PIN LED, i.e. mitigate the current crowding issue. Up to this point, 130 μm devices had been tested with great success. With larger devices, good uniformity, $\sim$75%, was also observed at 300 μm, as shown in Figure 3.9. This figure was produce using the
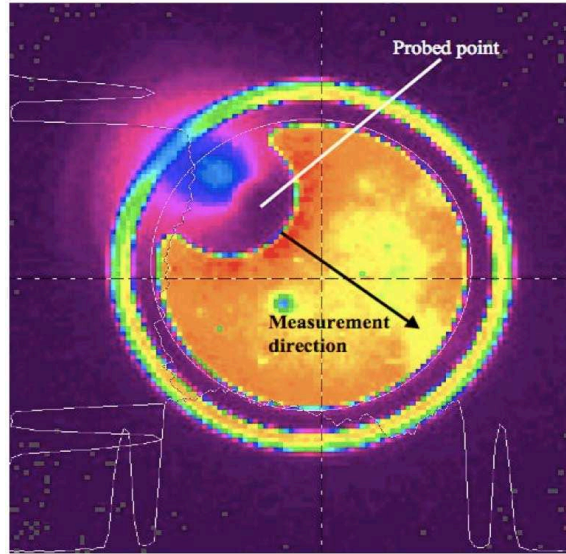
Figure 3.9:   A 300 μm device with a 5 μm Au metal contact ring. A 30 μm section in the upper left corner of the picture, quadrant II, is labeled "probe point." Measurements were taken, starting at the probe point and moving across the surface of the device. The probe point and the measurement direction are clearly labeled. This picture was taken with a 980M Spiricon IR camera using the laser beam analysis software from the manufacturer.

Spiricon image capture software to measure the pixel intensity across the surface of the device.

Analysis revealed that when the TAS increased, the beam uniformity across the 300 μm devices improved. This was expected for reasons stated earlier concerning the TJ as a scattering center and heat source. As the scattering center is moved away from the location where a multitude of carriers exist, the less impact it will have on those carriers.

Figure 3.9 shows a photo from the IR camera showing the beam profile of a device from wafer G2-3262, TAS =1742.5 Å. Figure 3.10 shows a plot of the emission across the surface of a device from wafer G2-3262.

A 25% drop in power was observed as the surface was measured across the device from the probe point. Wafer G2-3263 had devices that were inoperable and no discernable data was collected, but from the other wafers, several devices were extensively tested. Figure 3.11 shows a picture of a device from wafer G2-3161, TAS = 250.4 Å and Figure 3.12

50

Figure 3.10:   Beam uniformity plot across surface of 300 μm device. The plot is from data points measured across the device from the 30 μm section to the opposite side. A pixel intensity variation of 22% was observed across the surface of several devices.

shows a plot of the beam profile of the same device. Approximately, a 50% decrease in pixel intensity across the device is seen due to the thinner TAS layer.

3.2.2.2   TAS Layer Thickness vs Wavelength Shift.   Since the final device will be a resonant cavity structure, it was necessary to determine the amount of wavelength shift, resulting from heating, under forward bias. The DBR layers of the mirrors forming the cavity increase in thickness, due to heating caused by biasing, and thicker layers will produce a red-shift in the resonant wavelength. The index of refraction also changes due to the increase in heat, but to a lesser degree. Recall that the DBR layer thicknesses is equal to λ/4n. As each layer becomes thicker, so does the optical distance traveled by the reflected energy, causing a phase difference between the incident wave and the reflected wave, resulting in non-constructive reflection, or destructive interference. Hence the cavity is no longer able to sustain a standing wave at the emitted wavelength inside the cavity, i.e. no resonance at that wavelength, but it does have resonance at a longer wavelength, a red-shift has occurred in the cavity.

An investigation to determine the amount of red shift was conducted, and the amount of red shift was observed and noted such that the final device could be designed with a cavity that has a resonance at the expected red-shifted wavelength. These tests were conducted

51
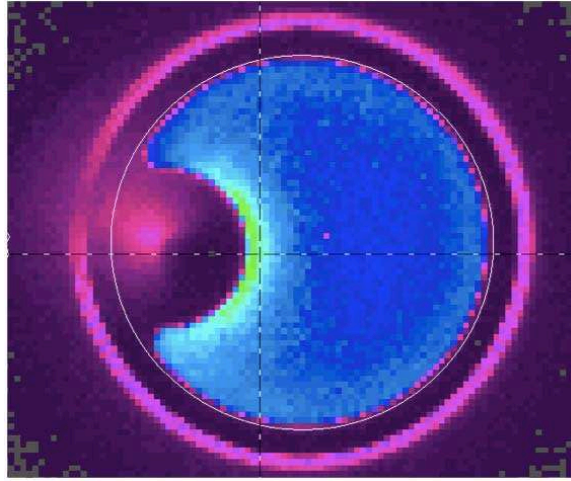
Figure 3.11:   A 300 μm device with 5 μm metal contact. The probe point and the measurement direction are the same as previously stated, from the probe point to the opposite side of the device. This picture was taken with a 980M Spiricon IR camera.
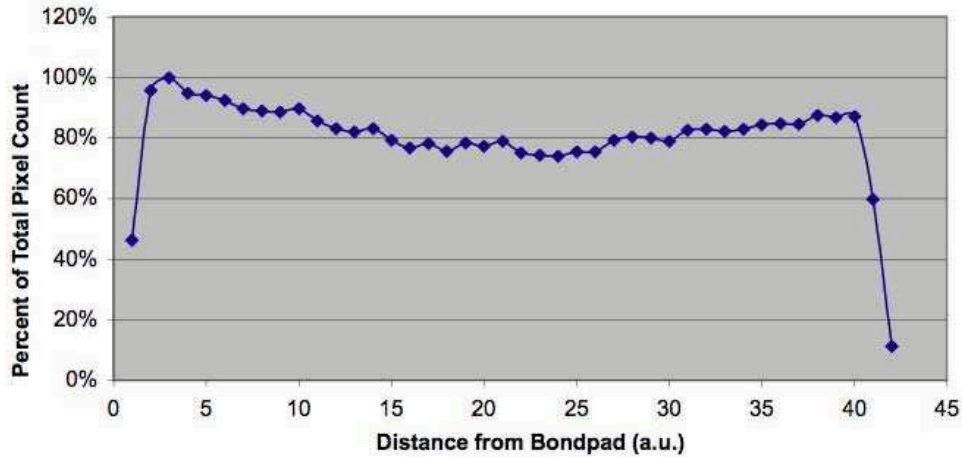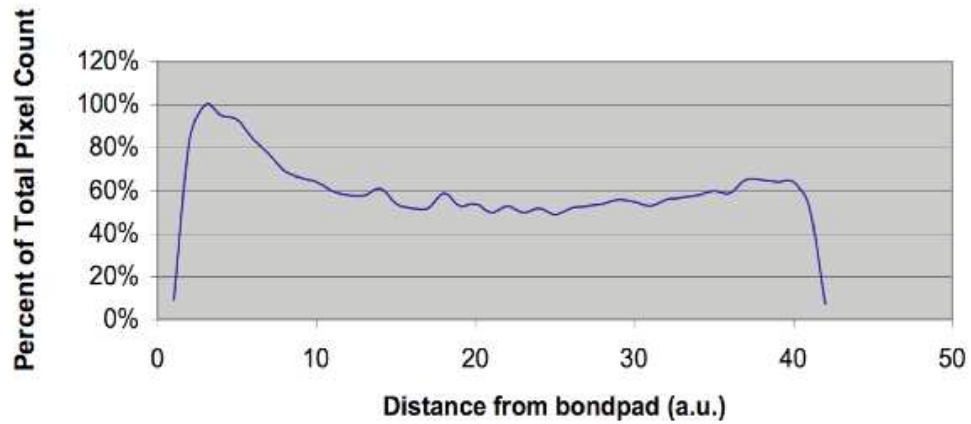

Figure 3.12:   Beam uniformity plot across surface of 300 μm device. The plot is from data points measured across the device from the probe point to the opposite side. A pixel intensity variation of nearly 50% was observed across the surface of several devices.

on the same TJ devices used for the TAS determination. Devices were grown with the TJ located in resonant intensity nodes within the, very low resonance, resonant cavity of the devices, created by utilizing two top ($R \sim 0.2\%$) and three bottom ($R \sim 1\%$) DBR pairs. Numerous devices were tested from wafers G2-3261 and G2-3262, to determine the wavelength shift. The device under test (DUT) is connected to an ILX Lightwave Model LDP 3811 Precision Pulsed Current Source, capable of reaching current levels of 500 mA. A silica multimode fiber (core diameter = 63 μm) is moved above the DUT in the probe station, to couple a portion of the emission and channel it into an OSA. In general, the devices selected for this experiment were the same devices used in the TJ location experiment.

Devices from wafer G2-3261, TAS = 250.0 Å, were damaged at current levels in the 215-220 mA range, and devices from wafer G2-3262, TAS = 1742.5 Å, were damaged at ~300 mA, so the injection current levels did not exceed these values for the respective devices tested. Five devices from each wafer were tested and average slopes were found. Figure 3.13 and Figure 3.14 show average slopes for devices from each wafer sample tested, with regression equations for each group showing the wavelength shift, the slope of the line, in nm/mA. The slopes of the regression equations are of the form $\Delta\lambda_0/\Delta I$, expressing the amount of wavelength shift due to current change.

Modeled data from Crosslight was generated for comparison with the measured values for this experiment as well. One would expect the red-shift to coincide with the increased injection current, as seen from the measured devices. With the model, no discernable differenced in the wavelength of the spontaneous emission was observed with varied current, but with a change in temperature, a very noticeable red-shift occurred. This occurred because no internal heating was used during the simulations. Attention is given to the spontaneous emission rate since spontaneous emission is the light producing phenomenon of interest in LEDs. Figure 3.15 shows plots of the spontaneous emission rates at 300 K and at 373 K.
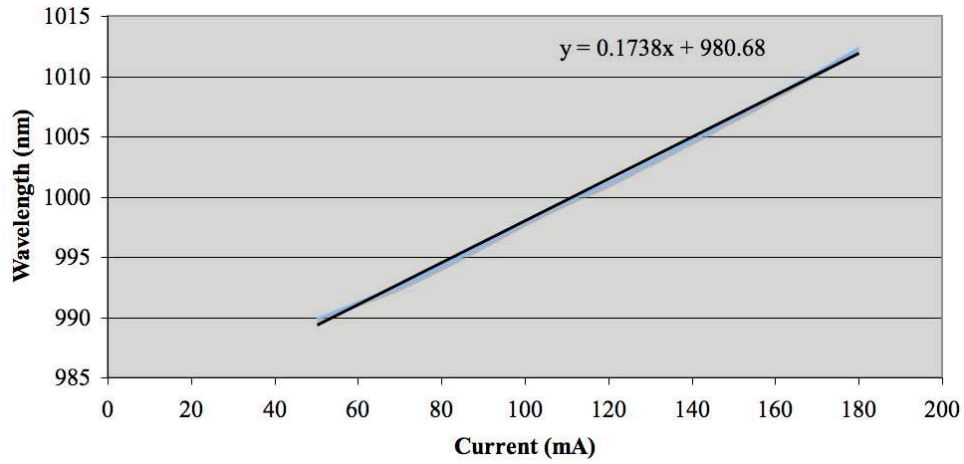
Figure 3.13:   The regression plot for devices from waver G2-3261, TAS = 250.4 Å. The average slope gives the wavelength shift per mA of current. For these devices, the amount of shift is $\frac{\Delta\lambda_0}{\Delta I}$ ~0.17 nm/mA.
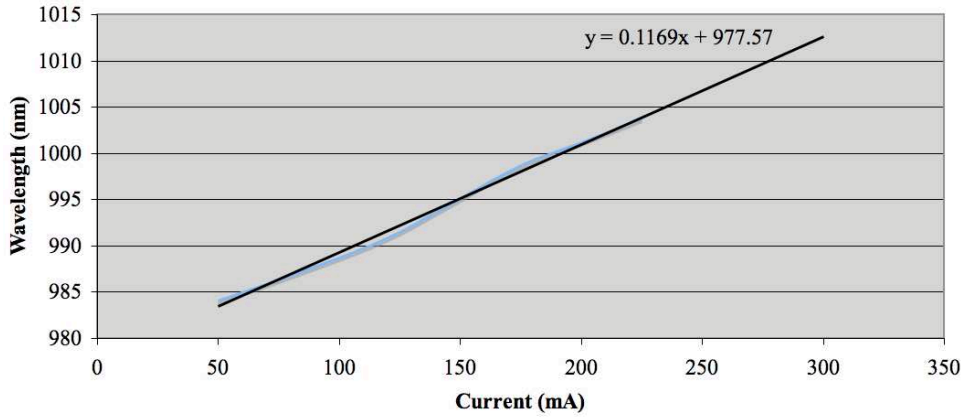
Figure 3.14:   The regression plots for devices from wafer G2-3262, TAS = 1742.5 Å. The average slope gives the wavelength shift per mA of current. For these devices, the amount of shift is $\frac{\Delta\lambda_0}{\Delta I}$ ~ 0.12 nm/mA.
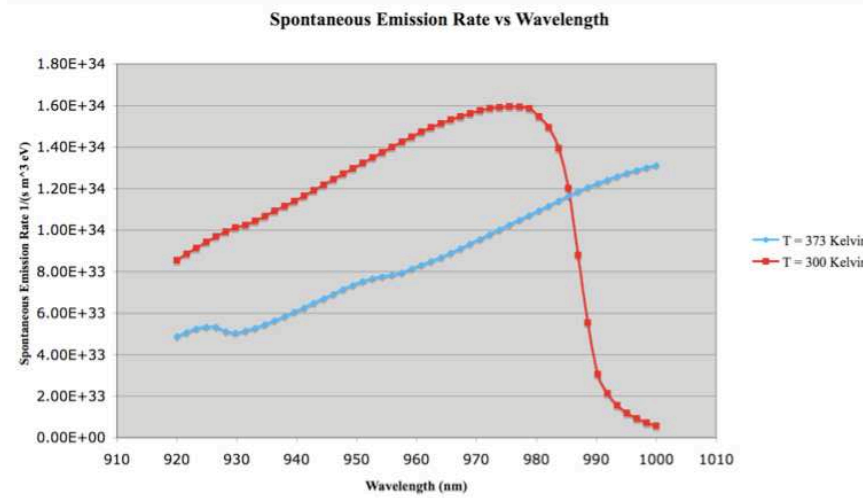
Figure 3.15: Spontaneous emission rate vs wavelength. Plots of modeled data generated at 300 K and 373 K, showing a red-shift (increase) in wavelength as the temperature increases. The red curve has a peak at 980 nm and the blue curve is shifted to peak value of ~1003 nm. Although this trend is observed from the temperature set by the user at the onset of model execution instead of with increase injection current level, it is consistent with the measured data collected.

Figure 3.15 shows that a thermally-induced red-shift does occur with an increase in temperature, in this case, it is the temperature established at the onset of the model execution (300 K), and the temperature due to injection current (373 K). A similar shift in wavelength existed in all modeled devices with various TAS values. A temperature increase is the result of an increase in injection current, and at a higher temperature, a shift in the spontaneous emission rate is seen. One can argue that the increase in temperature will be larger as the TJ is brought into closer proximity with the AR, and by varying the temperature during successive model executions, the model is effectively modeling the affect of temperature increases induced by larger injection currents, which results in a red-shift in wavelength emitted.

Table 3.3 shows the regression equations and slopes for each set of devices measured. It can be concluded that as the physical separation between the TJ and the AR (TAS) is increased, the amount of red-shift in wavelength emitted from the device reduces. This test concludes that the smallest red-shift of $\Delta\lambda_0/\Delta I = 0.12$ nm/mA occurs due to heating

Table 3.3: Identifies the wafer and the calculated slope. The trend shows that when the TJ is moved away from the AR, a smaller red shift occurs.

Wafer	TAS Thickness (Å)	Equation	$\frac{\Delta\lambda_0}{\Delta I}$ (nm/mA)
G2-3261	250.4	Y = 0.1738x + 980.676	0.17
G2-3262	1742.5	Y = 0.1169x+977.57	0.12

from a device with a TAS = 1742.5 Å, and the wavelength will change according to the regression equation

$$\lambda_0 = 0.1169I + 977.57 \tag{3.1}$$

where λ_0 is the design wavelength of interest in nm, and I is the injection current in A.

From the modeled data collected, the change in wavelength ($\Delta\lambda_0$) as a function of temperature change (ΔT) is

$$\frac{\Delta\lambda_0}{\Delta T} = \frac{(1003 - 980)}{(373 - 300)} = 0.315 \; nm/K \tag{3.2}$$

A relationship between the change in temperature (ΔT) as a function of the change in current (ΔI) can now be determined:

$$\frac{\Delta T}{\Delta I} = \frac{\Delta T}{\Delta\lambda_0} \frac{\Delta\lambda_0}{\Delta I} = 0.381 \; K/mA \tag{3.3}$$

3.2.2.3 TAS Layer Thickness vs Total Power. The final set of preliminary experiments was done to observe the affect of TAS thickness on the total output power. A silicon (Si) photodetector was attached to a Hewlett Packard Semiconductor Parameter Analyzer (SPA) to record the device output power. The detector was placed directly above the device at a distance about 1 cm. Although some energy may have been undetected due to the emission cone of the device, it is believed that over 95% of the energy was captured and measured. The SPA provided power for the detector and measured the optical energy,
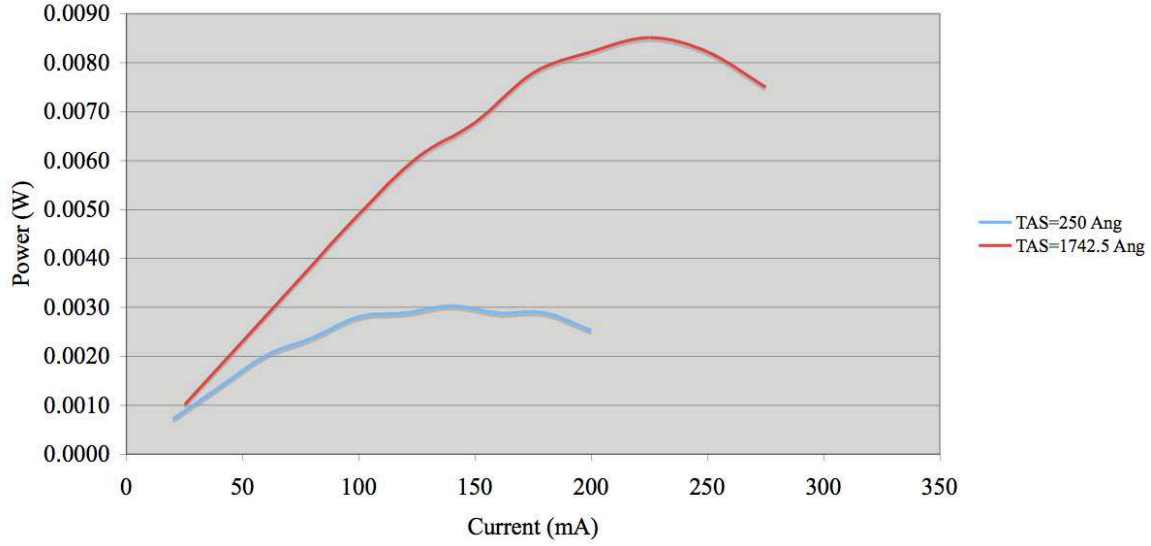
Figure 3.16: A plot of the total output power from two wafer samples with TAS = 250.0 Å for G2-3161 and TAS = 1742.5 Å for G2-3262. As the TAS increased, so does the total output power.

which was then converted to a current by the Si photodetector. A power conversion factor was used to convert the optical energy to get a power reading.

As in previous testing, several devices were extensively tested from each wafer. As the TAS was increased, the total output power increased, which suggests that the maximum TAS of 3045.0 Å is optimal. This could not be confirmed through testing because devices from wafer sample G2-3263 were inoperable. 3.16 shows average power versus current (L-I) curves for all devices tested. An increase in total output power of 5.5 mW, from 3 mW to 8.5 mW (~65%), occurred as TAS increased from 250.0 to 1742.5 Å.

Total power data was also generated using Crosslight®, for the 300 μm mesa devices at temperatures of 300 K and 384 K and different TAS values, and plotted in 3.17.

Modeled temperature values were selected based on the relationship described by 3.3, for current levels up to 300 mA, the maximum value used in the TAS layer characterization tests. 3.16 showed the maximum power occurring at ~225 mA. Using this value, the expected junction temperature is $\Delta T = 220$ x $0.381 = 83.8$ K. From a careful inspection of the plots, two observations can be made: 1) holding the TAS constant and varying the
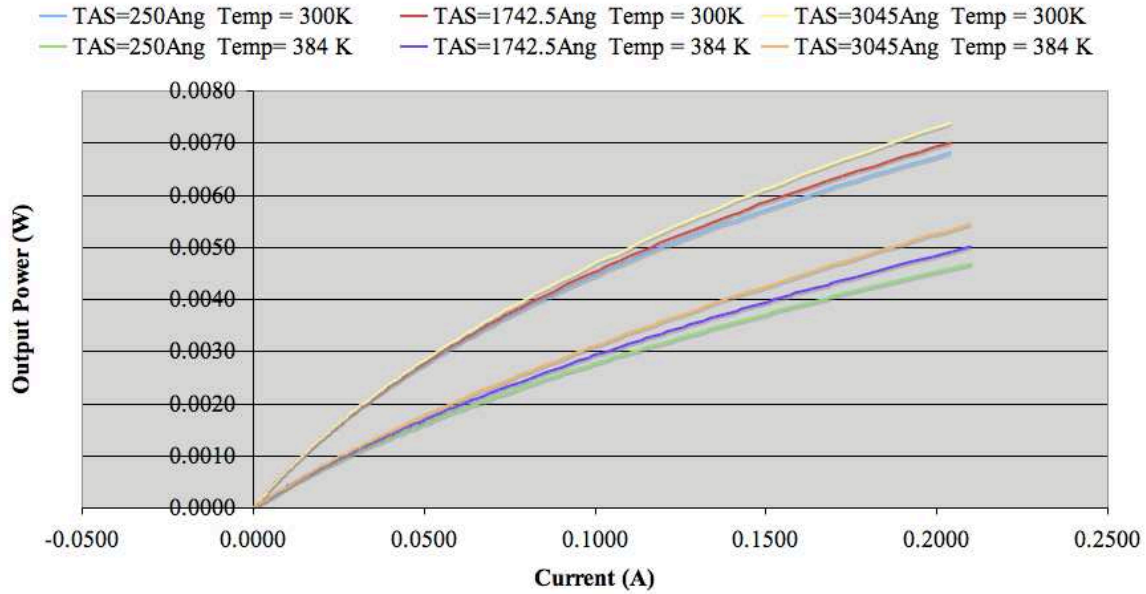
Figure 3.17: A plot of the total simulated device power of devices at 300 K and 384 K, with TAS at 250, 1742.5 and 3045 Å. As the TAS increased, so does the total output power. Another interesting observation was the significant decrease in output power with the change in temperature, which was on average about 2 mW.

temperature resulted in the most significant increase in output power, ~ 2 mW increase occurred with each device, an average increase of 40% per device; 2) holding the temperature constant and varying the TAS resulted in an increase in output power as the TAS increased, but to a smaller degree, $\sim$10% increase per device.

The modeled and measured data consistently express the same message that physical separation between the TJ and the AR improves the total output power from the device. There is a maximum TAS thickness, even though it was not identified during this study. As the TAS layer thickness is increased, the total cavity length will subsequently increase, which will reduce the overlap between the cavity resonant mode peaks and the spontaneous emission intensity, decreasing the overall device efficiency. One must keep in mind the various scattering mechanisms of the TJ, to include heating, electron and hole interband recombination centers (traps), and strong E-field, will impact the total output and, it has been demonstrated that separating the TJ and AR by a substantial distance reduces that impact.

3.3 Bipolar Cascade Light Emitting Diode Design

The data collected and analyzed from the preliminary tests directly lead to the final design of the STREMER. The research goal was to produce a wide area LED with a rectangular geometry having an aspect ratio of 0.006, and a minimum power rating large enough to deliver the needed energy on target for the HRIS. Efficiency is always a concern with semiconductor designs, but in this case, is a secondary issue.

The ideal structure consists of multiple ARs separated by TJs for current spreading and photon recycling. By stacking the ARs the total power is maximized, and as reported by Siskaninetz [27] three AR separated by a TJ made from a 200 Å n^{++} and a 200 Å p^{++} layer, grown one on top of the other, is the maximum number that can be utilized without affecting the emitted power. Adding a fourth stage resulted in a significant decrease in power. It is believed that this drop is due to total thermal impedance. Each active region is 380 Å and made of triple quantum wells, consisting of 60 Å undoped $In_{0.2}Ga_{0.8}As$ layers, separated by 100 Å undoped GaAs barriers.

Testing has shown that heating largely influences the operation of these devices. Equation 3.1 showed the wavelength shifts with increased injection current in 300 μm devices, and larger injection currents result in a larger shift in wavelength. Although the STREMER is expected to operate under a relatively large injection current, possibly on the order of 1 A, it has significantly larger surface area than devices previously tested. The larger area will dissipate more heat, resulting in a smaller shift in wavelength. This, coupled with heat sinking, will greatly reduce the device temperature even more, and subsequently the wavelength shift. Also, packaging techniques, referred to as *epi-side down* mounting, that extract significant amounts of heat, have been reported [37] [19] [32], with semiconductor lasers having injection current values much larger than 1.20 A. Comparison between epi-side up and epi-side down mounted devices show a reduction in wavelength shift of ∼30% [37] [19] [32]. Additionally, [36] shows significant heat dissipation by using gold-plated heat spreading layer on an etched-pillar device. Previous tests done in support of this work also show a large reduction in thermal resistance with an increase in device

size. In-spite of the lack of an actual operating wavelength at this juncture, device design can proceed using λ_0 instead, as detailed below, and the wavelength can be substituted after further thermal analysis is completed.

3.3.1   Device Modeling.   DBR mirrors are placed at the top and bottom of the stacked ARs forming a cavity. The top DBR is made of 4 pair of n-doped $Al_{0.5}Ga_{0.5}As$/ $Al_{0.9}Ga_{0.1}As$ layers each separated by a graded layer. The bottom layer is of the same composition but with 20 DBR pairs of n-doped material. The index of refraction of the high index layer, $Al_{0.5}Ga_0.5As$, is $n_h = 3.5$, while the index of refraction of the low index material, $Al_{0.9}Ga_{0.1}As$, is $n_l = 3.2$. Using these indicies, each individual DBR layer thickness, (d), as a function of λ_0, can be determined:

$$d_h = \frac{\lambda_0}{4(3.52)} = 0.0714\lambda_0 \tag{3.4}$$

$$d_l = \frac{\lambda_0}{4(3.20)} = 0.0781\lambda_0 \tag{3.5}$$

and λ is therefore

$$\lambda = \frac{\lambda_0}{n_{GaAs}} = \frac{\lambda_0}{3.5} = 0.284\lambda_0 \tag{3.6}$$

where λ_0 is in nm.

For the microcavity to sustain a standing wave, or have a resonance, the wave must have nodes at the mirror surfaces. For this reason, the cavity length must be integer multiples of $u\frac{\lambda}{2}$, where u is an integer number. Additionally, each of the three ARs need to be in a resonance peak antinodes for the most efficient transfer of energy, and each TJ should be placed in a node, since it is a large scattering center. To design the cavity, multiple AR-TAS-TJ sections are used. Figure 3.18 shows one of the AR-TAS-TJ sections used to build the cavity. Each section is designed with a TAS layer that is $\frac{3}{4}\lambda - \frac{1}{2}(AR + TJ)$, to make sure the AR and the TJ is appropriately placed.
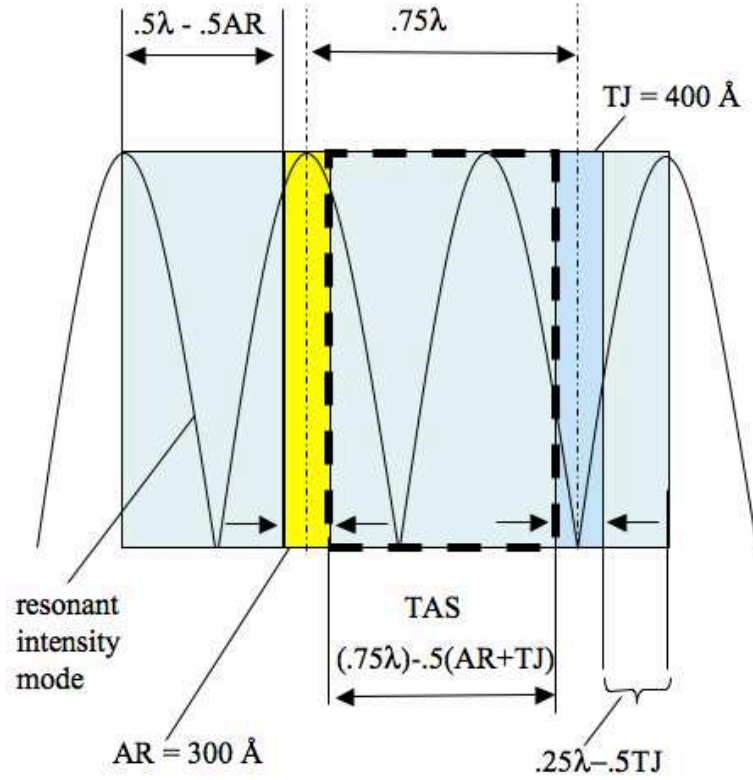
Figure 3.18: Notional depiction of a section of the STREMER microcavity. Shown are the constituents: AR and TJ with the requisite spacing in between for the least TJ impact. The resonant intensity mode is shown, with the AR in an antinode and the TJ in a node. This section is $\frac{3}{2}\lambda$ long.
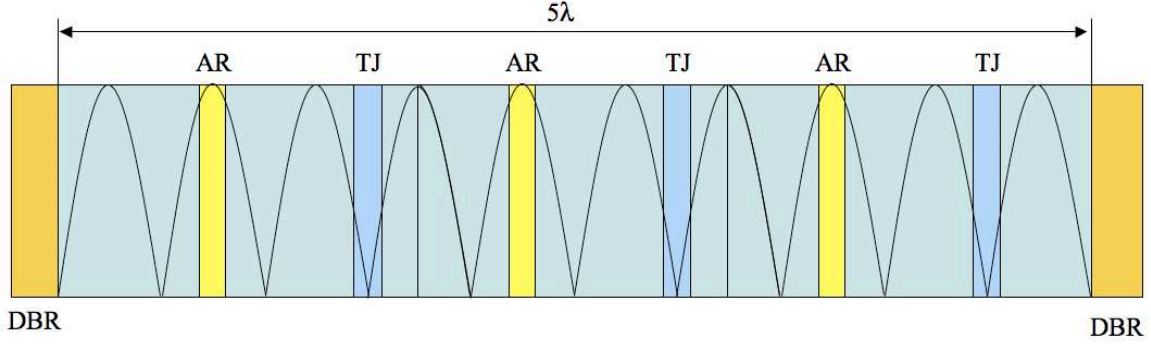
Figure 3.19:   Notional depiction of the STREMER full-sized microcavity. Shown are the constituents: AR and TJ with the requisite spacing in between for the least TJ impact. The resonant intensity mode is shown, with the AR in an antinode and the TJ in a node. This cavity is $\frac{10}{2}\lambda$, or 5λ long.

For a three stage device, three sections are necessary, making the total cavity $\frac{10}{2}\lambda$ long. The full cavity design is depicted in 3.19, and the energy band diagram is shown in 3.20. Clearly distinguishable features include the multiple QW and the TJ, which comprise each stage.

Consider the case where the STREMER operates at injection current levels up to 1 A, and using no heat sinking, so the design wavelength is calculated using 3.1:

$$\lambda_0 = \quad 0.1169(1000 \ A) + 977.6 \qquad (3.7)$$

$$\lambda_0 = \qquad 1094.5 \ nm$$

Table 3.4 shows the values needed to design a basic STREMER without heat sinking, which were also the values used to model the final device.

The modeled, final device produced the LI characteristic shown in Fig. 3.21. This LI curve is for a 200 μm modeled STREMER, and shows a drive current up to 500 mA, and output power of $\sim$9 mW. The STREMER is expected to operate under drive currents much larger than 500 mA, and produce much larger output power, due to the larger device dimensions and proper heat sinking. Physical devices, with the same dimensions, but no

62
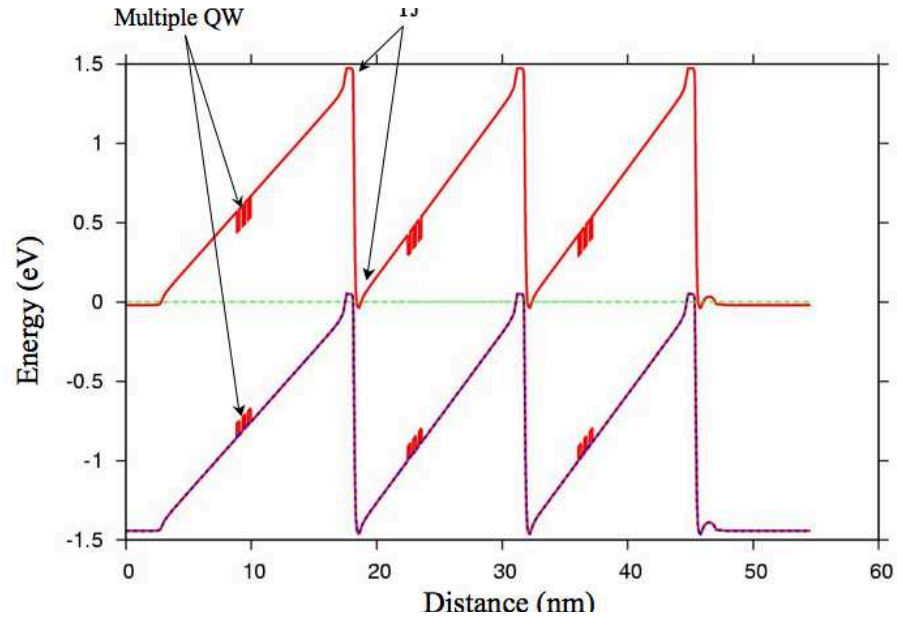
Figure 3.20: The energy band diagram for the three stage, BC-RCLED STREMER, produced using Crosslight. The multiple QW and TJ, of each stage, is clearly labeled.

Table 3.4: STREMER design values based on 1 A injection current and no heat sinking.

$\lambda_0 = 10945$ Å	
Parameter	Value (Å)
DBR layer - low index	857.7
DBR layer - high index	772.7
TAS layer thickness	1941.9
Cavity length	15546.9
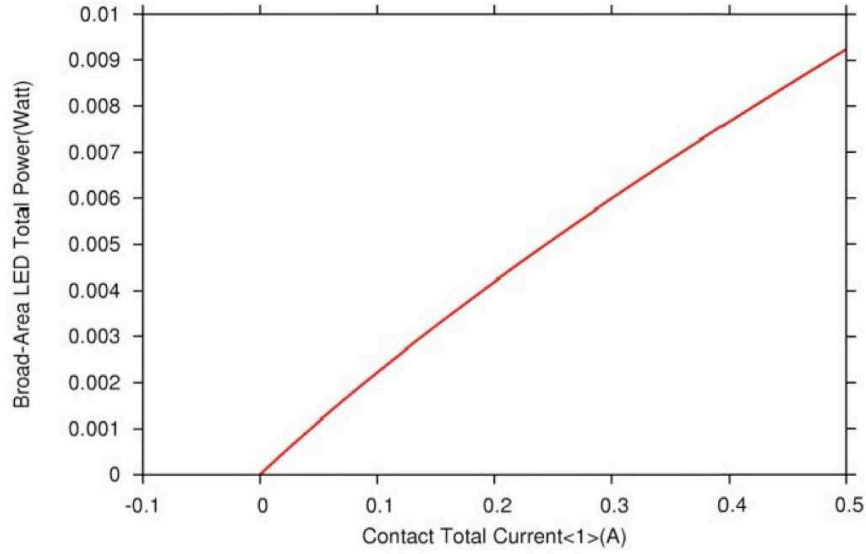
Figure 3.21: Modeled total power output from the STREMER device. This shows that for a 200 μm device, at a drive current of 500 mA, the total output power is $\sim$9 mW.

resonant cavity, were tested with drive currents up to 300 mA, producing output power of $\sim$3.17 mW. Closer inspection of Fig. 3.21 shows that at 300 mA, the output power of the modeled STREMER is $\sim$6.5 mW, almost double the measured value, but of the same order of magnitude. It is believed that not modeling the effect of heat, in the model devices, account for the difference between the measured and modeled values.

A qualitative analysis was performed based on reports detailing the demonstrated scalability of vertical cavity devices, in this case lasers, in an arrayed format [17]. It has been reported that devices in an arrayed configuration show linear power scaling, limited, in general, by thermal roll-over [36]. Borrowing from this fact and operating under the hypothesis that it is conceivable that if several of the 200 μm devices tested, which produced an output power of 3.2 mW, are placed in an array that matches the surface area of a single STREMER section, which is 140 x 10000 μm, or 0.014 cm^2, a power scaling calculation can arrive at a value that is relatively close to what could be expected. Again, heating is an issue, and this calculation does not take that into consideration, and it also assumes uniform injection current. To equal the area of a STREMER section, 35 of the 200 μm devices would be necessary, and if each produced an output power of 3.2 mW, the total output from

a section would be 112 mW. Likewise, a much larger current would be necessary to drive this much larger device. Again using the scaling assumption to perform the calculation, if each device required 200 - 300 mA, the much larger section would require drive currents on the order of 7 - 10 A, which is not unheard of for high-power devices [21].

The information obtained from each of these tests was key to determining the physical characteristics of the final STREMER device. Several key findings include: 1) having a TAS that physically separates the TJ and AR, but allows the TJ to remain in a resonant intensity node is desirable, 2) growing the highly doped n^{++} and p^{++} layers under low temperature created a TJ with the best slope efficiency compared to other growth processes used, 3) because heat will be generated within the device, a thermally induced wavelength shift will occur in the amount of ~1 ÅmA of drive current for TAS=1742.5 Å. Since a resonant cavity will be used, it must be designed to accommodate that shift, 4) the total output power is directly proportional to the TAS, 5) it is theoretically possible to produce 140 μm x 10000 μm STREMER sections with output power levels of over 100 mW.

For an illuminator to be suitable for the HRIS, it needs to be designed and fabricated as follows: TJs should be used as current spreading layers to prevent current crowding that reduces the total output power from the device; multiple AR, separated by TJs, are needed to increase the total output power from the device; the layers forming the TJ should be grown at 575 °C for best TJ characteristic slope under reverse bias; the TAS should be 1742.5 Å or about $\frac{3}{4}\lambda - \frac{1}{2}(AR + TJ)$, which allows the TJ to be placed in a node, and provides adequate separation between the TJ and the AR to minimize the affect of the TJ on the total output power and the uniformity of the device; the cavity needs to be designed to sustain a resonant wavelength that is the result of a thermally induced red shift. By adopting these characteristics, an optimized STREMER can be developed to meet the requirements of the imaging system.

3.3.2 Device Fabrication. All material growths, fabrication and testing was completed in-house. Although several wafer samples were grown for preliminary experiments, a material growth for the final BC-RCLED design was not accomplished. The device was

Table 3.5:   The fabricated devices tested, identified by their label. Also shown is the structure of the device tested.

Wafer Label	Device Structure
G2-3039	*p-i-n* Structure
G2-3069	4 stage BCLED
G2-3152	1 stage BCLED
G2-3181	3 stage BCLED
G2-3262	Low resonance BC-RCLED

instead modeled with Crosslight Finite Element Modeling software utilizing the data collected from the preliminary investigations. The fabricated devices tested did not have the resonant cavity structure, however, the TJ was inserted as a spreading layer and for photon recycling in the multi-stage devices. These BC-LED wafers were used to fabricate devices for final characterization, and the wafers processed and their structural makeup, are shown in Table 3.5.

All devices were fabricated using material that was epitaxially grown with a Varian Gen II MBE system. The sample wafer material used included a *p-i-n* LED, 2, 3, and 4 stage BCLEDs. The *p-i-n* structure is a standard diode, and the remaining devices fabricated were BC-LEDs with Esaki TJs incorporated. The TJs were formed by growing a heavily doped n^{++} layer on a heavily doped p^{++} layer. The layers were degenerately doped so that the conduction band in the n^{++} material is approximately even with the valence band in the p^{++} material. This allows electrons to tunnel through the narrow barrier that results from such extreme band bending due to the high doping. A three-step process was designed to produce the STREMERs and several wide area square mesas for further TJ investigations. The sizes of the square mesas were 80, 110, 140, 170, 200, and 250 μm, and were selected to bridge the gap from previous tests by Siskaninetz [29] on devices of 50 μm and myself on 300 μm devices. The STREMERs were designed with 150, 200 and 250 μm wide mesas, and lengths of 500, 1000, 2000, 4000, and 10000 μm. These stripe sizes were selected so that they can be combined to form the requisite aspect ratio during packaging. Table 3.6 shows the required length needed to produce the proper aspect ratio for a given device width.

Table 3.6:   The required device lengths to create the proper aspect ratio of 0.006 given the device width.

Width (μm)	Required Length (mm)
150	25
200	33
250	42

From previous experimentation, current crowding has been observed when probing mesas on the top of the stack. Due to this effect, an extra processing step was added to the STREMER's process to insert an isolation layer. A conformal contact was used that started at the base of the device and traveled along it's sides up to the top of the mesa, where it contacted the semiconductor surface. A SiN isolation layer was placed between the metal contact layer and the wafer surface, including the side-walls of the device. The isolation layer isolates the metal from the semiconductor surface in all areas except for the top of the stack over a 25 μm area around the top of the mesa. This forces current to flow only at that contact point. As shown in Figure 3.22, the metal overlaps the SiN and makes contact with the top of the mesa around the top perimeter, leaving an open aperture. The SiN is also deposited along the mesa sides and at the base, extending outward from the mesa's base, about 50 μm, to allow probing and bonding.

Figure 3.23 shows an intensity reading from the Sprircom 980M IR camera, displaying the beam profile from a 500 μm device. A 130 μm wide metal contact is used to probe the device. Evidence of current crowding can be observed under the metal contact, with a majority of the electrons injected into the device traveling directly beneath the metal, while some migrate outside the metal width before recombining. This causes the non-uniform emission pattern from the device shown. It's believed that an isolation layer will help prevent electrons from entering the device beneath the probe strip and, thus increase the uniformity of the beam by mitigating current crowding.

The device fabrication process is not given in detail in this report [31]. The devices were fabricated using standard cleaning and photolithography procedures, using inductively coupled plasma etching, electron-beam evaporation and various sputtering meth-
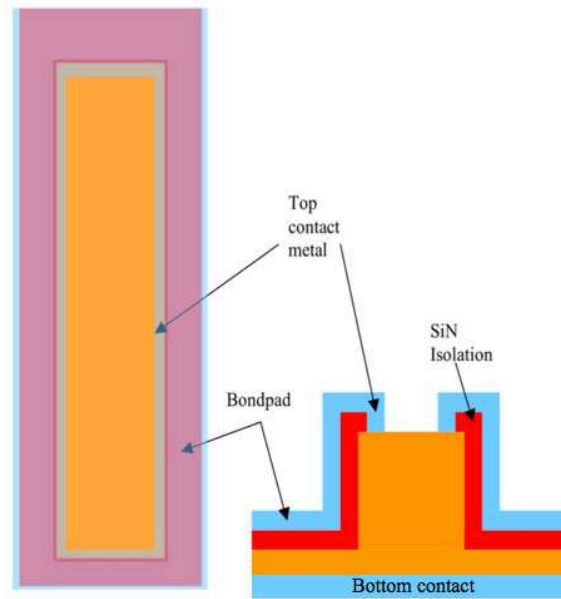
Figure 3.22:   A depiction of the STREMER shown from the top and side view. An isolation layer is between the top metal contact and the wafer surface except for on the top of the mesa.
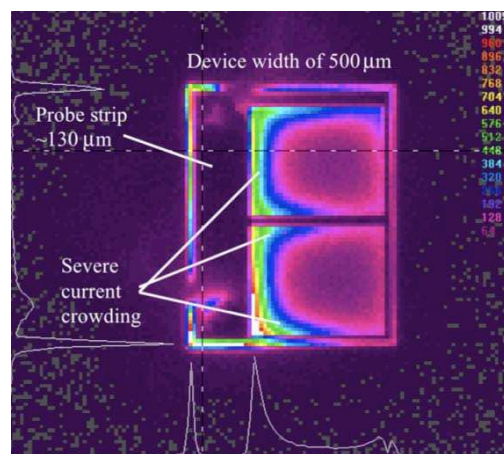
Figure 3.23:   An intensity plot of a 500 μm, single stage device, with   130 μm wide metal contact. Evidence of current crowding can be seen under the metal contact. A large amount of radiative recombination occurs while very few electrons and holes recombine and produce light in other parts of the device.

ods for metallization. The standard p-metal recipe used at this facility is a Ni/Ge/Au/Ni/Au stack. Instead of this stack, an n-metal deposition was initially adopted, which consisted of Ti/Au, since the Ge sputter target was damaged during earlier processing. The p-metal produced a non-ideal ohmic contact, but current was still able to be injected into the devices for characterization. Metallizations performed by E-beam evaporation deposits a discontinuous metal layer at the top and the base of the mesa. This is due to the large mean free path of gas molecules at high vacuum, making the evaporation a highly directional deposition technique. Since a continuous, conformal layer is needed, approximately 6000 Å of Ti/Pt/Au was sputtered on the surface of the wafer. The backside of the wafer was evaporated with the same metal composition. A second series of devices were later fabricated with the proper n-metal composition.

Figure 3.24 shows a depiction of the final packaged device; with three of the 150 μm x 10000 μm devices used to create the desired aspect ratio. Multiple wire bonds are shown, and are used to enhance the uniformity across the devices. During the packaging of the final devices, a problem with the metal contacts on the surface and the back of the wafer adhering to the semiconductor was discovered. Although some tests were done on the STREMER sections with drive current up to 500 mA, STREMER power tests could not be accomplished, nor could a current rating be determined, due to a metal adherence problem. Thus final determinations had to be inferred from the data collected for the devices tested.

3.3.3 Device Characterization.   The final testing results for the beam uniformity versus current density investigation, total power tests, and the remote sensing demonstration follow. Data was measured and modeled with Crosslight$^{®}$ to determine final values in each case.

3.3.3.1 Beam Uniformity vs Current Density.   Single stage BC-LEDs were used to investigate the current spreading capability of the TJ in devices with mesa widths ranging from 110 to 250 μm. An IR camera was used to capture a pixilated image of the beam exiting the device. An average relative variance was calculated for each device tested, with all values having arbitrary units. The total current handling capability was determined
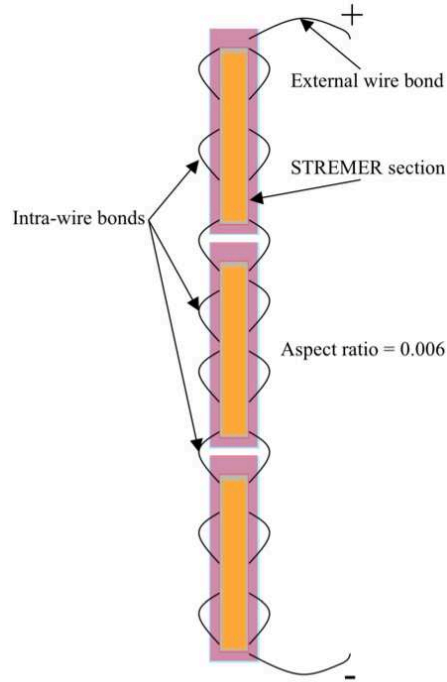
Figure 3.24:   Depiction of the STREMER showing wirebonding patterns and the leads for current injection.

by gradually increasing the drive current from 10 mA up to device failure or when roll-over occurred. Since this experiment was done to assess the beam uniformity only, total power out is not a concern, and no power measuring instrumentation was utilized; the pixel intensity registered by the camera was used to determine roll-over. A series of gray scale pictures of the optical emission from the devices were produced using the Spiricon camera, where each pixel in the image captured by the camera, has a gray scale value that corresponds to the relative optical intensity emitted from the device. A bright gray colored pixel corresponds to a relatively large optical intensity being delivered to that pixel, while a darker gray pixel corresponds to a relatively small optical intensity being delivered. Several pictures depicting beam profiles from several devices, at various current injection levels, were produced and used for statistical analysis to determine the relative beam profile variance for each device . An in-house developed code was used to analyze the gray scale pictures captured by the Spiricon 980M. The camera measures pixel intensity and the in-house code records the grayscale value of each pixel. Each pixel value is then used to calculate a mean-pixel and variance value across the device surface. These mean and variance values are

assigned to each picture, making it possible to quantify the uniformity of the beam across that surface. An average relative variance is calculated for each set of devices, according to size, with all values having arbitrary units. Typically, the application determines what is an acceptable variance in beam uniformity. Although for this specific application, 3-D remote sensing, a strict adherence to uniformity values is not required. A 20 - 25% variability was determined to be acceptable.

For each device size group, the current density values where the variance approaches the accepted cuttoff value range, 0.20-0.25, as shown in Table 3.7. Table 3.7 shows how the variance changes with device size and current density. To determine what a typical current density might be, consider the OSRAM LEDs. A device having a current rating of 1 A, a surface area of 1×10^{-4} cm^2, creates a current density of approximately 1×10^7 mA/cm^2. Using this as a benchmark, the current densities were calculated for the in-house developed devices. Table 3.7 also lists the device sizes and the current densities, for comparison with a benchmark value calculated using the OSRAM LEDs. From Table 3.7, it can be concluded that the 110 and 140 μm devices have current densities near the benchmark, and maintain a variance lower than ~ 0.25. It can also be seen that a larger current density is possible in the 100 μm device, while maintaining a good relative variance, ~ 0.20-25. This analysis assumes that 1×10^6 mA/cm^2 is a typical drive current density for devices of this size, per the OSRAM current rating. The uniformity of the OSRAM device is not known and cannot be compared or commented on. Figure 3.25 shows a gray-scale image of a 140 μm device taken by the Spiricon IR camera. There are noticeable darker regions near the center of the device, which indicates that a smaller intensity is emitted from the center than that occurring at the edges. This particular device has a relative variance of ~ 0.21 at a current density of $\sim 9.2 \times 10^5$ mA/cm^2.

3.3.3.2 Total Power Measurements. Total power measurements are part of the characterization experiments done on all devices. Modeling was a key part in the determination of the total power of the in-house developed devices. For the total power measurements, an integrating sphere was used, along with a digital multimeter and a 40 A

71

Table 3.7:   Current density for all device sizes at the point where the relative variance surpasses the accepted range, 0.20-0.25. The 110 μm devices failed before larger current densities could be achieved. Only devices 110 μm and 140 μm have current densities that are near the benchmark value.

Device Size (μm)	Variance	Current Density (mA/cm^2)
110	0.15	1,983,471
140	0.23	991,736
170	0.25	415,225
200	0.31	175,000
250	0.26	48,000

Figure 3.25:   A gray-scale IR image of a one-stage 140 μm device under forward bias. Pixel intensities are shown, with a noticeable variation between the edges and the center of the device. The lighter grey edges indicate a higher optical intensity.

current source, to record the maximum total output power from all devices tested. The devices were mounted using a custom designed holder, and abutted to the opening of the sphere. The integrating sphere collects the energy and converts it into current, which is measured by the DMM. This current is then multiplied by a conversion factor, and a final value for the total optical power is obtained. The conversion factor at 940 nm has a value of 1.454 x 10^{-4} A/W.

Because the STREMER is an experimental device, additional testing was conducted prior to the power measurements. The STREMERs are devices made from smaller sections, with final devices that are relatively large, having a longest dimension of about 2.5 cm. Each individual section was probed to verify proper functionality. The ILX current source, with a maximum drive current of 500 mA, was used to drive the devices. This setup used a micro-

140 x 1000 μm

Figure 3.26:   A 150 μm x 1000 μm STREMER under a 500 mA drive current. A neutral density filter, ND = 1.0, is placed in front of the camera collecting the energy emitted from this device to prevent detector saturation.
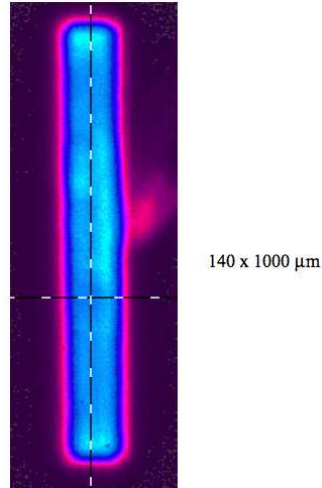
scope directly above the devices to allow near field imaging. The maximum current from the ILX was sufficient to adequately drive only the 1000 and 2000 μm long STREMER devices to high level injection. This was determined by viewing the intensity image from the IR camera. Devices larger than 2000 μm, only showed intensities that were qualitatively about one-half of the intensity level captured by the smaller devices, indicating that the 500 mA current source was not sufficient to push the STREMER into a high level injection condition. Figure 3.26 shows a 150 x 1000 μm device under a 500 mA drive current with a neutral density filter, ND = 1, in place over the camera's detector to prevent detector saturation.

Again, there was difficulty achieving good adherence between the gold metal contact layer, the silicon nitride isolation layer, and the semiconductor surface using the available sputtering and evaporation systems used in device fabrication. Multiple attempts were made to adjust the deposition process for better adhesion, without success. For this reason, remote sensing demonstrations using the STREMERS could not be accomplished, but valuable data was obtained from using the OSRAM LEDs in the remote sensing demonstration.

73

3.4   Summary of Results

The work completed over the course of this study has demonstrated the use of an Esaki TJ as an effective current spreading layer in large area LEDs. The TJ has been studied and used in other applications, but none have quantified the upper limit of it's ability to perform current spreading in large-area LEDs. By setting a minimum variability in uniformity across a device, in this case 0.25, and a minimum current density, in this case 1×10^6 A/cm^2, we have determined that a mesa width of 140 μm is the maximum size at which our TJ could maintain effectiveness as a current spreading layer. The TJ is a key enabling technology in the development of the wide-area STREMER, because it permits the fabrication of a device capable of producing a energy pattern with an aspect ratio of 0.006, and a relatively uniform emission from the device.

This work has also produced a design for a large area BC-RCLED (STREMER) for integration into the HRIS prototype, eliminating the need for multi-gimbaled point or line scanners, or the need to utilize a bank of point scanners. By synthesizing the Esaki TJ, DBR mirrors to form a RC, MAR, and MQW into an LED, we have developed a device with a very large surface area, expected to have relatively good beam uniformity, deliver energy in a relatively narrow emission cone (30° or less), and deliver an output power of over 330 mW. Using this device as the illuminator for the HRIS, the data acquisition time is greatly reduced, because the entire FOV can be acquired with only one sweep of the area, which cannot be done with current scanners. Lastly, we have demonstrated that the STREMER is an effective, active illuminator for the HRIS, by performing a scaled remote sensing demonstration.

Although the TJ has many benefits, it does come with some limitations. Since it is a scattering center, it needs to be properly placed relative to the AR, to limit it's negative affect on device efficiency. Experiments to minimize this impact were conducted when the TJ was placed in multiple positions relative to the AR (the TAS distance) and the total output power was measured. It was clear that as the TJ was moved away from the AR, the total output power increased, suggesting that the maximum TAS possible is most desirable.

Table 3.8:   Current density for all device sizes at the point where the relative variance surpasses 0.20. The 110 μm devices failed before larger current densities could be achieved. Only devices 110 μm and 140 μm have current densities that are near the benchmark value.

Device Size (μm)	Variance	Current Density (mA/cm^2)
110	0.15	1,983,471
140	0.23	991,736
170	0.25	415,225
200	0.31	175,000
250	0.26	48,000

Device designers utilizing TJs must still be mindful that if they are placed inside a resonant cavity, the TJ must be located in resonant intensity nodes for best device efficiency. This could cause the cavity to become very large, depending on the number of stages being used, creating other issues that can arise when using large vertical cavities, like reduced energy transfer efficiency between optical emission and the resonant intensity wave inside the cavity, reducing the device efficiency.

Testing showed that the TAS also impacted the beam uniformity across the surface of the device. During this testing, the TAS was varied and the uniformity of the beam was recorded, while holding the device size constant. It was concluded that as the TAS was increased, the uniformity improved. With the TAS = 1742.5 Å, uniformity across the surface of the device was ∼80%, and with the TAS = 250.0 Å, beam uniformity decreases to less than 50%. Since beam uniformity is directly tied to current crowding, it was suggested that the TJ would be a good current spreading layer for wide area LEDs. Although this was not the primary purpose for using a TJ in these devices, spreading was a beneficial by-product. A correlation between the current density and the variation in uniformity across the device was found, as shown in Table 3.8. For current densities smaller than those shown in the table, which correspond to a larger device area. Larger relative variance values were seen, which suggests that a larger beam nonuniformity will be the result. From this current density-relative uniformity variance relationship, it could be concluded that the 140 μm device is the largest device in-which the TJ can function as a good current spreading layer, in this case, one producing a relative variance of 20 - 25% or better.

Plots of various design parameters were produced to guide development of the final HRIS. Parameters include, detector quantum efficiency (η_{det}), detector integration time (τ_{int}), system range (R), and source power rating (P$_{source}$). For a given SNR and R, one can determine P$_{source}$ based on η_{det} and τ_{int}. Additionally, R can be extended, using the same source, by adjusting η_{det} and τ_{int}. For this particular case, given an SNR of 20 dB, and a R of 5000 cm, and assuming $\eta_{det} = 0.6$ and $\tau_{int} = 0.033$ sec, an LED source needs to have a power rating ≥ 321 mW.

A key part of this effort was to design the BC-RCLED STREMER, with a unique emission surface area in a rectangular format, having a width-to-length aspect ratio of 0.006, that can be used as an illuminator for the hybrid range-intensity sensor. From the data collected from this investigation, an optimized STREMER design could be determined. Figure 3.27 shows the STREMER cavity design. The STREMER has a $10\lambda/2$ cavity, three TJ-AR-TAS stages within the cavity, with the TJs in resonant intensity nodes, and the ARs in resonant intensity antinodes. To ensure that the TJ and the AR is properly placed, the TAS layer must be $\frac{3}{4}\lambda - \frac{1}{2}(AR + TJ)$, where λ is the operating wavelength adjusted for the heat induced red-shift. The bottom highly reflective DBR consists of twenty pair of alternating layers of Al$_{0.5}$Ga$_{0.5}$As and Al$_{0.9}$Ga$_{0.1}$As, creating a mirror with reflectivity of nearly 100%.

The top DBR is the output coupler of the device, and consists of four pair of alternating layers of the same structural constituency as the bottom DBR structure, with a reflectivity of around 75%. To construct an efficient mirror to sustain resonance at the red-shifted wavelength, the layers of the DBRs need to be $0.0714\lambda_0$ for the Al$_{0.5}$Ga$_{0.5}$As layer, and $0.0781\lambda_0$ for the Al$_{0.9}$Ga$_{0.1}$As layer. The physical dimensions of the STREMER designed for the hybrid sensor is 140 μm x 3000 μm. These values create the necessary aspect ratio, 0.006, to deliver a stripe down range with dimensions 18 cm x 3000 cm. The STREMER is a set of three rectangular devices, as shown in Figure 3.28. A 200 μm STREMER was modeled and produced a total output of $\sim$9 mW. Total power measured was compared to the total power modeled, and revealed a discrepancy of $\sim$17% between the modeled and actual values, suggesting the total power of a 200 μm STREMER BC-RCLED is $\sim$7.8 mW
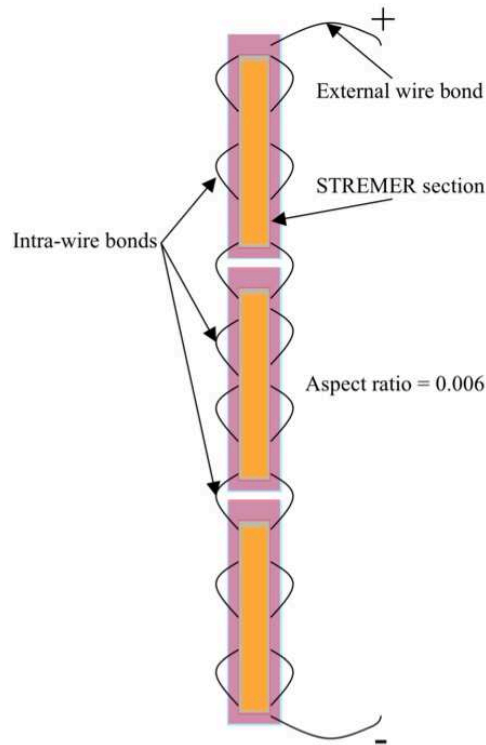
Figure 3.27: STREMER cavity design. This is a three-stage device with TJs placed in resonant intensity nodes and the ARs in antinodes. The bottom DBR, on the left, is a 20-pair stack and the top DBR, on the right, is a 4-pair stack. The cavity is $10\lambda/2$ long.

at 500 mA. Power scaling analysis reveals that it is possible to produce a STREMER device with total output power over 300 mW. The device's emission cone could not be modeled with the current version of Crosslight®, so no conclusive modeled data can be presented showing how the resonant cavity reduces the emission cone.

With the sensor system mounted on an autonomous ground vehicle, a likely incidence angle of 1.54 rad would be created. Under this, worst case condition, the STREMER delivers sufficient energy to the target, meeting the 20 dB SNR requirement, provided a collection optic of 15 cm or larger is used, with a detector having an integration time of 330 msec and quantum efficiency of 60% or better.

Development of an in-house emitter with the proper aspect ratio of 0.006 was accomplished, but wafer growth could not be completed. Although fabrication and testing on STREMER devices of the BCLED variety was accomplished, packaging for total power de-
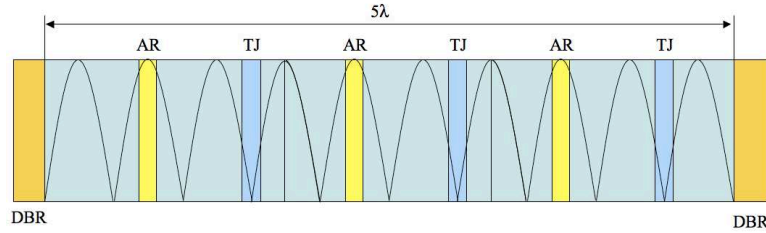
77

Figure 3.28: The schematic of the STREMER. The STREMER is made of three smaller devices, connected vertically, to create the required aspect ratio. It is wire bonded around its perimeter to improve beam uniformity.

termination, current handling capability, as well as the remote sensing demonstration, could not be accomplished because of inadequate adhesion between the metal contact layer and the SiN isolation layer. This limitation needs to be overcome to complete the device characterization. Deposition of conformal metal on conformal SiN has neither been a primary focus of this effort, nor the focus of the researchers at this facility, so a suitable process did not exist. An alternative isolation layer could be silicon dioxide. Processing could have caused the problem, so a process to ensure greater adherence of conformal metal to conformal SiN needs to be developed.

Bibliography

1. Carlsson, C., H. Martinsson, R. Schatz, J. Halonen, and A. Larsson. "Analog Modulation Properties of Oxide Confined VCSELs at Microwave Frequencies". *J. Lightwave Technol.*, 20(9):1740–1749, September 2002.

2. Choquette, K., J. Klem, A. Fischer, O. Blum, A. Allerman, S. Kurtz I. Fritz, W. Breiland, K. Geib R. Sieg, J. Scott, and R. Naone. "Room temperature continuous wave InGaAsN quantum well vertical-cavity lasers emitting at 1.3 μm". *Elect. Lett.*, 36(16):1388–1390, 2000.

3. Chuang, S. L. *Physics of Optoelectronic Devices*. Wiley, New York, 1995.

4. Coldren, L. A. and S. W. Corzine. *Diode Lasers and Photonic Integrated Circuits*. Wiley, New York, 1995.

5. Esaki, L. "Discovery of the Tunnel Diode". *IEEE Trans. of Electr. Dev.*, 23:7, 1976.

6. Feld, S., J. Loehr, R. Sherriff, J. Wiemeri, and R. Kaspi. "In-Situ Optical Monitoring of AlAs Wet Oxidation Using a Novel Low-Temperature Low-Pressure Steam Furnace Design". *IEEE Photon. Tech. Lett.*, 10(2):197–199, February 1998.

7. Getty, J., E. Skogen, L. Johansson, and L. Coldren. "CW Operation of 1.55-μm Bipolar Cascade Laser with Record Differential Efficiency, Low Threshold, and 50-Ω Matching". *IEEE Photon. Tech. Lett.*, 15(11):1513–1515, November 2003.

8. Jackson, H.D. *Frequency Response Characterization of Multiple Quantum-Well $In_{0.20}Ga_{0.80}As$ Semiconductor Lasers Operating at High-Temperatures*. Master's thesis, University of Dayton, 2002.

9. Kim, J., E. Hall, O. Sjölund, G. Almuneau, and L. Coldren. "Room-Temperature, Electrically-Pumped Multiple-Active-Region VCSELs with High Differential Efficiency at 1.55 μm". *Elect. Lett.*, 35(13):1084–1085, June 1999.

10. Kjebon, O., R. Schatz, S. Lourdudoss, S. Nilsson, and B. Stålnacke. "Modulation Response Measurements and Evaluation of MQW InGaAsP Lasers of Various Designs". *SPIE 2684*, 138–152. 1996.

11. Knödl, T., M. Golling, A. Straub, and K. Ebeling. "Multi-Diode Cascade VCSEL with 130% Differential Quantum Efficiency at CW Room Temperature Operation". *Elect. Lett.*, 37(1):31–33, January 2001.

12. Knödl, T., M. Golling, A. Straub, R. Jager, R. Michalzik, and K. Ebeling. "Multistage Bipolar Cascade Vertical-Cavity Surface-Emitting Lasers: Theory and Experiment". *IEEE J. Select. Topics Quantum Electron.*, 9(5):1406–1414, September/October 2003.

13. Knödl, T., R. Michalzik, M. Golling, and K. Ebeling. "Current-Spreading-Induced Bistability in Bipolar Cascade Vertical-Cavity Surface-Emitting Lasers". *Appl. Phys. Lett.*, 81(4):583–585, July 2002.

14. Koda, R., C. Wang, D. Lofgreen, and L. Coldren. "High-Differantial-Quantum-Efficiency, Long-Wavelength Vertical-Cavity Lasers Using Five-Stage Bipolar-Cascade Active-Regions". *Appl. Phys. Lett.*, 86:211104, 2005.

15. Loehr, J., W. Siskaninetz, J. Wiemeri, and S. Feld. "Optical Communications for Avionics". *IEEE Aerospace and Electronic Systems Magazine*, 13(4):9–12, April 1998.

16. Mayer, P., F. Rana, and R. Ram. "Photon Noise Correlations in Electrically Coupled Semiconductor Lasers". *Appl. Phys. Lett.*, 82(5):689–691, February 2003.

17. Miller, M., M. Grabherr, R. Jager, M. Kicherer, F. Mederer, and K. J. Ebeling. "kW/cm2 VCSEL Arrays for High Power Applications". K. D. Choquette and C. Lei (editors), *Vertical-Cavity Surface-Emitting Lasers IV*, volume 3946. 2000.

18. Moller, C., J. Bottcher, M. Protsch, and H. Kunzel. "GaAs-based tunnel junctions for micro-cavity devices". *All-Optical Networking: Existing and Emerging Architecture and Applications/Dynamic Enablers of Next-Generation Optical Communications Systems/Fast Optical Processing in Optical Transmission/VCSEL and Microcavity Lasers. 2002 IEEE/LEOS Summer Topical Meeting*, MH5–17 – MH5–18, 2002.

19. Page, H., A. Robertson, C. Sirtori, C. Becker, G. Glastre, and J. Nagle. "Demonstration of ($\lambda \sim 11.5$ μm) GaAs-based quantum cascade laser operating on a Peltier cooled element". *Photonics Technology Letters, IEEE*, 13(6):556–558, 2001.

20. Patterson, S., G. Petrich, R. Ram, and L. Kolodziejski. "Continuous-Wave Room Temparature Operation of Bipolar Cascade Laser". *Elect. Lett.*, 35(5):395–397, March 1999.

21. Qu, Yi, Shu Yuan, Chong Yang Liu, Baoxue Bo, Guojun Liu, and Huilin Jiang. "High-power InAlGaAs/GaAs and AlGaAs/GaAs semiconductor laser arrays emitting at 808 nm". *Photonics Technology Letters, IEEE*, 16(2):389–391, 2004.

22. Schmid, W., D. Wiedenmann, M. Grabherr, R. Jager, R. Michalzik, and K. Ebeling. "CW Operation of a Diode Cascade InGaAs Quantum Well VCSEL". *Elect. Lett.*, 34(6):553–555, March 1998.

23. Siskaninetz, W. *Net Modal Gain Analysis of High-Frequency In$_{0.20}$Ga$_{0.80}$As Semiconductor Lasers Operating at High-Temperatures*. Master's thesis, University of Dayton, 1998.

24. Siskaninetz, W., J. Ehret, J. Albrecht, R. Bedford, T. Nelson, and J. Lott. "Gigahertz Modulation of GaAs-Based Bipolar Cascade Vertical Cavity Surface-Emitting Lasers". *Optics Lett.*, 32(2):136–138, 2007.

25. Siskaninetz, W., J. Ehret, T. Dang, J. Van Nostrand, J. Lott, and T. Nelson. "Reduced Power Consumption in GaAs-Based Bipolar Cascade Lasers". *Elect. Lett.*, 38(21):1259–1261, 2002.

26. Siskaninetz, W., J. Ehret, and J. Griffith. "Bipolar Cascade Lasers: Direct-Drive Lasers for RF-Photonic Links". *Great Lakes Photonics Symposium*, GL106–24. SPIE, June 2006.

27. Siskaninetz, W., J. Ehret, J. Lott, J. Griffith, and T. Nelson. "Enhanced Performance Of Bipolar Cascade Light Emitting Diodes By Doping the Aluminum Oxide Apertures". *Appl. Phys. Lett.*, 86(11):111108, 2005.

28. Siskaninetz, W., J. Ehret, J. Lott, and T. Nelson. "GHz Operation of Bipolar Cascade VCSELs". *Conference on Lasers and Electro-Optics, CLEO2006*, CWG1. OSA/LEOS, May 2006.

29. Siskaninetz, W., J. Ehret, S. Maley, J. Griffith, J. Lott, and T. Nelson. "Improved Luminescence in Light-Emitting Diodes Using Esaki Tunnel Junctions". *Frontiers in Optics 2005, 89th OSA Annual Meeting and Laser Science Conference XXI*, FThE4. OSA/APS, October 2005.

30. Siskaninetz, W., H. Jackson, J. Ehret, J. Wiemeri, and J. Loehr. "High-Temperature High-Frequency Operation of Single and Multiple Quantum Well In$_{0.20}$Ga$_{0.80}$As Semiconductor Lasers". *Solid State and Diode Laser Technology Review*. DEPS, May 2001.

31. Siskaninetz, W. J. *Bipolar Cascade Vertical-Cavity Surface-Emitting Lasers for RF Photonic Link Applications*. Ph.D. thesis, Air Force Institute of Technology, 2007.

32. Tsekoun, A., R. Go, M. Pushkarsky, M. Razeghi, C. Kumar, and N. Patel. "Improved performace of quantum cascade lasers via manufacturable quality epitaxial side down mounting process utilizing aluminum nitride heatsinks". M. Razeghi and G. J. Brown (editors), *Quantum Sensing and Nanophotonic Devices III*, volume 6127. 2006.

33. Turner, R. J. *A Wide Area Bipolar Cascade Resonant Cavity Light Emitting Diode for a Hybrid Range-Intensity Sensor*. Ph.D. thesis, Air Force Institute of Technology, 2008.

34. Wierer, J., P. Evans, N. Holonyak, and D. Kellogg. "Lateral Electron Current Operation of Vertical Cavity Surface Emitting Lasers with Buried Tunnel Contact Hole Sources". *Appl. Phys. Lett.*, 71(24):3468–3470, December 1997.

35. Wierer, J., D. Kellogg, and N. Holonyak. "Tunnel Contact Junction Native-Oxide Aperture and Mirror Vertical-Cavity Surface-Emitting Lasers and Reesonant-Cavity Light-Emitting Diodes". *Appl. Phys. Lett.*, 74(7):926–928, February 1999.

36. Wipiejewski, T., M. G. Peters, B. J. Thibeault, D. B. Yound, and L. A. Coldren. "Size-dependent output power saturation of Vertical-Cavity Surface-Emitting Laser diodes". *IEEE Photon. Tech. Lett.*, 8(1):10–12, 1996.

37. Xingsheng, L., M. H. Hu, K. N. Hong, C. G. Caneau, M. H. Rasmussen, Jr. R. W. Davis, and Z. Chung-En. "Comparison between epi-down and epi-up bonded high-power single-mode 980-nm semiconductor lasers". *Advanced Packaging, IEEE Transactions on [see also Components, Packaging and Manufacturing Technology, Part B: Advanced Packaging, IEEE Transactions on]*, 27(4):640–646, 2004.